

Stellar Wind Variations During the X-ray High and Low States of Cygnus X-1^{1,2}

D. R. Gies^{3,4}, C. T. Bolton⁵, R. M. Blake⁵, S. M. Caballero-Nieves³, D. M. Crenshaw³,
P. Hadrava⁶, A. Herrero⁷, T. C. Hillwig⁸, S. B. Howell⁹, W. Huang^{4,10}, L. Kaper¹¹,
P. Koubský⁶, and M. V. McSwain^{12,13}

¹Based on observations with the NASA/ESA Hubble Space Telescope obtained at the Space Telescope Science Institute, which is operated by the Association of Universities for Research in Astronomy, Incorporated, under NASA contract NAS5-26555. These observations are associated with programs GO-9646 and GO-9840.

²Based on data obtained at the David Dunlap Observatory, University of Toronto.

³Center for High Angular Resolution Astronomy, Department of Physics and Astronomy, Georgia State University, P. O. Box 4106, Atlanta, GA 30302-4106; gies@chara.gsu.edu, scaballero@chara.gsu.edu, crenshaw@chara.gsu.edu

⁴Visiting Astronomer, Kitt Peak National Observatory, National Optical Astronomy Observatory, operated by the Association of Universities for Research in Astronomy, Inc., under contract with the National Science Foundation.

⁵David Dunlap Observatory, University of Toronto, P. O. Box 360, Richmond Hill, Ontario, L4C 4Y6, Canada; bolton@astro.utoronto.ca

⁶Astronomical Institute, Academy of Sciences of the Czech Republic, Fričova 298, CZ-251 65 Ondřejov, Czech Republic; had@sunstel.asu.cas.cz, koubsky@sunstel.asu.cas.cz

⁷Instituto de Astrofísica de Canarias, 38200, La Laguna, Tenerife, Spain; Departamento de Astrofísica, Universidad de La Laguna, Avda. Astrofísico Francisco Sánchez, s/n, 38071 La Laguna, Spain; ahd@ll.iac.es

⁸Department of Physics and Astronomy, Valparaiso University, Valparaiso, IN 46383; todd.hillwig@valpo.edu

⁹WIYN Observatory and National Optical Astronomy Observatory, P. O. Box 26732, 950 N. Cherry Ave., Tucson, AZ 85719; howell@noao.edu

¹⁰Department of Astronomy, California Institute of Technology, MC 105-24, Pasadena, CA 91125; wenjin@astro.caltech.edu

¹¹Astronomical Institute Anton Pannekoek, Universiteit van Amsterdam, Kruislaan 403, 1098-SJ Amsterdam, The Netherlands; lexx@science.uva.nl

¹²Department of Physics, Lehigh University, 16 Memorial Drive East, Bethlehem PA 18015; mcswain@lehigh.edu

¹³Guest investigator, Dominion Astrophysical Observatory, Herzberg Institute of Astrophysics, National

ABSTRACT

We present results from *Hubble Space Telescope* ultraviolet spectroscopy of the massive X-ray and black hole binary system, HD 226868 = Cyg X-1. The spectra were obtained at both orbital conjunction phases in two separate runs in 2002 and 2003 when the system was in the X-ray high/soft state. The UV stellar wind lines suffer large reductions in absorption strength when the black hole is in the foreground due to the X-ray ionization of the wind ions. A comparison of the *HST* spectra with archival, low resolution spectra from the *International Ultraviolet Explorer Satellite* shows that similar photoionization effects occur in both the X-ray high/soft and low/hard states. We constructed model UV wind line profiles assuming that X-ray ionization occurs everywhere in the wind except the zone where the supergiant blocks the X-ray flux. The good match between the observed and model profiles indicates that the wind ionization extends to near to the hemisphere of the supergiant facing the X-ray source. We also present contemporaneous spectroscopy of the H α emission that forms in the high density gas at the base of the supergiant's wind and the He II λ 4686 emission that originates in the dense, focused wind gas between the stars. The H α emission strength is generally lower in the high/soft state compared to the low/hard state, but the He II λ 4686 emission is relatively constant between X-ray states. The results suggest that mass transfer in Cyg X-1 is dominated by the focused wind flow that peaks along the axis joining the stars and that the stellar wind contribution from the remainder of the hemisphere facing the X-ray source is shut down by X-ray photoionization effects (in both X-ray states). The strong stellar wind from the shadowed side of the supergiant will stall when Coriolis deflection brings the gas into the region of X-ray illumination. This stalled gas component may be overtaken by the orbital motion of the black hole and act to inhibit accretion from the focused wind. The variations in the strength of the shadow wind component may then lead to accretion rate changes that ultimately determine the X-ray state.

Subject headings: binaries: spectroscopic — stars: early-type — stars: individual (HD 226868, Cyg X-1) — stars: winds, outflows — X-rays: binaries

1. Introduction

The massive X-ray binary Cygnus X-1 is a seminal target in the study of gas dynamics in the vicinity of a stellar mass black hole. Its X-ray luminosity and energetic jets (Gallo et al. 2005) are powered by gas accretion from the nearby companion star HD 226868 (O9.7 Iab; Walborn 1973) in a spectroscopic binary with a 5.6 day orbital period. There are several ways in which mass transfer from the supergiant to the black hole may occur in this system (Kaper 1998). The O-supergiant, like other massive and luminous stars, has a strong radiatively driven wind that may be partially accreted through the gravitational force of the black hole. The supergiant is large and is probably close to filling its critical Roche surface (Gies & Bolton 1986a; Herrero et al. 1995), so a gas stream through the inner L1 point may also be present. The actual gas flow in the direction of the black hole is probably intermediate between a spherically symmetric wind and a Roche lobe overflow stream, and there is evidence that the flow is best described as a focused wind (Friend & Castor 1982; Gies & Bolton 1986b; Gies et al. 2003; Miller et al. 2005). The gas ions responsible for accelerating the wind may become ionized in the presence of a strong X-ray source, leading to a lower velocity, “stalled” wind (Blondin et al. 1990; Stevens 1991). In situations of very high X-ray flux, photoionization may extend so close to the supergiant’s photosphere that the wind never reaches the stellar escape velocity and thus ceases to become an X-ray accretion source (Day & Stevens 1993; Blondin 1994). However, such a high X-ray flux may heat the outer gas layers to temperatures where the thermal velocities exceed the escape velocity to create a thermal wind that may fuel black hole accretion.

Important clues about the mass transfer process come from the temporal variations of the observed X-ray flux. Cyg X-1 is generally observed in either a low flux/hard spectrum state, with an X-ray spectrum that is relatively flat, or a high flux/soft spectrum state with a steeper power-law spectrum (Shaposhnikov & Titarchuk 2006). The gamma-ray portion of the spectrum is also elevated during the high/soft state (McConnell et al. 2002). The high/soft state usually lasts for periods of days to months, and the fraction of time observed in the high/soft state has increased from 10% in 1996–2000 to 34% since early 2000 (Wilms et al. 2006). This increase may be related to an overall increase in the supergiant’s radius in the period from 1997 to 2003 – 2004 that is suggested by changes in the long term optical light curve (Karitskaya et al. 2006a). The system sometimes experiences so-called failed-state transitions, when it starts to increase in flux, but then stops at an intermediate state and returns to the low/hard state. All these transitions probably reflect changes in the inner truncation radius of the accretion disk surrounding the black hole that are caused by a variable accretion rate (largest when the system is in the high/soft state; Done 2002; McClintock & Remillard 2006). Thus, the temporal variations in the X-ray state offer us the means to compare the black hole accretion processes with observational signatures related

to mass transfer.

The H α emission formed in the high density gas at the base of the stellar wind is an important diagnostic of the mass loss rate in massive stars (Puls et al. 1996; Markova et al. 2005). The H α emission variations in HD 226868 over the last few years are documented in independent spectroscopic investigations by Gies et al. (2003) and Tarasov, Brocksopp, & Lyuty (2003). Both of these studies concluded that the H α emission appears strongest when the system is in the low/hard X-ray state, while a range of weak to moderate emission strengths are observed during the high/soft states. This is a surprising result, since taken at face value, strong emission is associated with a large wind mass loss rate, and the simplest expectation that the X-ray accretion flux increases with mass loss rate is, in fact, not observed. There are several possible explanations: (1) A denser wind may be more opaque to X-rays. However, this seems unlikely because the observed inverse relation between H α emission strength and X-ray flux is observed at all orbital phases, not just when the supergiant and its wind are in the foreground. (2) The X-ray source may photoionize and heat the gas responsible for the H α emission, so that a larger X-ray flux leads to a decrease in H α strength. This clearly occurs at some level, but both Gies et al. (2003) and Tarasov et al. (2003) argue that portions of the wind shaded from the ionizing flux also display significant temporal variations. (3) Changes in the X-ray flux will lead to variations in the ionized volume of gas surrounding the black hole, and consequently, the total acceleration of the wind in the direction towards the black hole will vary with the distance traveled before the atoms responsible for line-driving are ionized. Thus, a stronger, denser wind might reach a faster speed before ionization, and since the Bondi-Hoyle accretion rate varies as $\sim v^{-4}$, the gas captured by the black hole (and the associated X-ray flux) declines.

This last process can be tested through direct study of the degree of wind ionization observed in the ultraviolet P Cygni lines formed in the supersonic part of the wind outflow. When the system is observed with the ionization region in the foreground, the absorption cores of these P Cygni lines will be truncated at a blueshift corresponding to the highest projected speed before encountering the ionization zone, the so-called Hatchett-McCray effect (Hatchett & McCray 1977). The binary is so faint in the ultraviolet that high dispersion spectra were very difficult to obtain with the *International Ultraviolet Explorer (IUE)* satellite (Davis & Hartmann 1983), but a good series of observations were obtained with *IUE* at lower spectral resolution that clearly indicate the weakening of the wind lines when the black hole is in front (Treves et al. 1980; van Loon, Kaper, & Hammerschlag-Hensberge 2001). Most of these spectra were obtained in the low/hard X-ray state (§5), when according to the varying wind strength model the mass loss rate is higher and the wind is less ionized and faster.

We embarked on a new program of high S/N, high dispersion UV spectroscopy to test this hypothesis with the *Hubble Space Telescope* Space Telescope Imaging Spectrograph (STIS). We obtained observations at the two orbital conjunction phases in both 2002 and 2003. These sets of observations were both made during the rare high/soft X-ray state, and planned observations during the low/hard state were unfortunately scuttled by the STIS electronics failure in 2004. However, we can rebin the high quality *HST* spectra made during the high/soft state to the lower resolution of the *IUE* archival spectra (mostly low/hard state) in order to test whether or not the wind ionization state does in fact differ significantly between states. We describe a program of supporting optical spectroscopy we have obtained to check the orbital phase (§2) and wind strength (§3) at the times of the *HST* observations. We compare the H α measurements with the contemporaneous X-ray light curve recorded with the *Rossi X-ray Timing Explorer* All-Sky Monitor instrument (Levine et al. 1996) and confirm our earlier result showing how H α tends to strengthen as the X-ray flux declines (§3). We then describe the observed variations in the main UV wind lines and present a simple “shadow wind” model for the profiles (§4). We compare the variations observed in the *HST* and *IUE* spectra in §5, and then reassess the question of the mass transfer process in §6. We will discuss the photospheric features in the UV spectra in a forthcoming paper (Caballero Nieves et al., in preparation).

2. Observations and Orbital Ephemeris

The *HST* STIS spectra were obtained with the first-order G140M grating in a series of subexposures at different grating tilts in order to record the UV spectrum over the full available range (1150 to 1740 Å). Two full sets were made near each orbital conjunction phase in runs in both 2002 and 2003. All the spectra were reduced using the IDL software developed at NASA Goddard Space Flight Center for the STIS Instrument Definition Team. The spectra were rebinned on a $\log \lambda$, heliocentric wavelength scale to a spectral resolution of $R = 10000$ and rectified to a pseudo-continuum based upon the flux in relatively line-free regions.

The space observations were supported by contemporaneous, ground-based observations of the red spectrum in the vicinity of H α . These 125 spectra were made with the University of Toronto David Dunlap Observatory 1.88 m telescope, NOAO Kitt Peak National Observatory 0.9 m coudé feed telescope, Herzberg Institute of Astrophysics Dominion Astrophysical Observatory 1.85 m telescope, and the Academy of Sciences of the Czech Republic Astronomical Institute Ondřejov Observatory 2 m telescope. We also obtained a smaller set of 22 blue spectra that record the variations in the He II $\lambda 4686$ line that probably

forms in the focused part of the wind (Gies & Bolton 1986b; Ninkov, Walker, & Yang 1987; Karitskaya et al. 2006b). A summary of all these observing runs is given in Table 1 that lists run number, range of heliocentric Julian dates of observation, spectral range recorded, spectral resolving power ($R = \lambda/\Delta\lambda$, where $\Delta\lambda = \text{FWHM}$ of the line spread function), number of spectra obtained, and details about the telescope, spectrograph, and detector. The spectra were reduced and transformed to rectified flux on a uniform heliocentric wavelength scale (as described in Gies et al. 2003).

Most of the red spectra also record the He I $\lambda 6678$ absorption line, and we decided to measure the stellar radial velocity from this line to check on the orbital ephemeris at the time of the *HST* observations. The radial velocities were measured in the same way as outlined by Gies et al. (2003) by fitting a Gaussian to the central line core. For the sake of completeness, we also measured the radial velocity of the supergiant from the *HST* UV spectra using a cross-correlation method (Penny, Gies, & Bagnuolo 1999) with an *IUE* spectrum of HD 34078 as the reference template. The results are presented in Table 2 (given in full in the electronic version) that lists the heliocentric Julian date of mid-observation, orbital phase, radial velocity and its associated error, observed minus calculated velocity residual, $\text{H}\alpha$ equivalent width, and the corresponding run number from Table 1. We note that independent measurements of the He I $\lambda 6678$ line in the Ondřejov spectra using the KOREL package (Hadrava 2007) led to fully consistent results.

We computed orbital elements from these velocities (omitting those from *HST*) using the non-linear, least-squares fitting method of Morbey & Brosterhus (1974). We made a circular orbital fit with the period fixed at the value obtained by Brocksopp et al. (1999) from data spanning a 26 yr interval. Our results are compared to those from Brocksopp et al. (1999) and from Gies et al. (2003) in Table 3, and they are consistent with these earlier studies. The current epoch for the time of supergiant inferior conjunction $T(\text{IC})$ occurs 0.017 ± 0.012 days later than the prediction from Brocksopp et al. (1999), and we will adopt this revised epoch for the definition of orbital phase throughout the paper. We omitted the *HST* measurements from the orbital solution because of concerns about possible systematic differences in the velocities derived from the UV lines and He I $\lambda 6678$, but the ($O - C$) residuals for the *HST* measurements given in Table 2 show that the UV measurements are in reasonable agreement with the velocity curve derived from He I $\lambda 6678$.

3. Wind and X-ray States During the *HST* Observations

The optical red spectra were obtained with the primary goal of monitoring the gas density at the base of the stellar wind of the supergiant. The $\text{H}\alpha$ observations of HD 226868 are

summarized in two panels in Figure 1 according to the X-ray state at the time of observation (see Fig. 2 below). The top portions show plots of the profiles arranged by orbital phase while the lower grayscale images show the spectral flux interpolated in radial velocity and orbital phase. The white line in the lower image shows the radial velocity curve of the supergiant (Table 3). These figures show that most of the emission/absorption complex appears to follow the orbit of the supergiant as expected for an origin in the supergiant wind. We measured the $H\alpha$ equivalent width in the same way as before (Gies et al. 2003) by making a numerical integration over a 40 \AA range centered on $H\alpha$, and these measurements are listed in column 6 of Table 2. We estimate that the typical measurement error is $\pm 0.1 \text{ \AA}$ (depending mainly on the S/N ratio of the individual spectrum).

We show the time evolution of the $H\alpha$ equivalent width for a total of 240 measurements from Gies et al. (2003) and the new observations in the top panel of Figure 2. The lower panel of this figure shows the daily average soft X-ray flux over the same interval from the All-Sky Monitor on the *Rossi X-ray Timing Explorer* (Levine et al. 1996). These flux measurements are the quick-look results provided by the *RXTE*/ASM team¹⁴. The two arrows in the top panel indicate the times of the two *HST* observing runs, which took place when Cyg X-1 was in the high/soft state. The new measurements confirm the trends described by Gies et al. (2003) and Tarasov et al. (2003) that the $H\alpha$ emission tends to be stronger when the soft X-ray flux declines and that there is a considerable range in emission strength when the soft X-ray flux is large (see Fig. 1).

Figures 3 and 4 show a detailed view of the time evolution of the $H\alpha$ emission strength and X-ray flux for the week surrounding the *HST* runs in 2002 and 2003. The bottom panels in these figures show the X-ray fluxes in both the low energy ($1.5 - 3 \text{ keV}$; + signs) and higher energy ($5 - 12 \text{ keV}$; \times signs) bands for the individual, 90 s exposure, dwell measurements. Unfortunately, both the $H\alpha$ and X-ray measurements are not exactly coincident in time with the *HST* observations, so we have made a time interpolation between the closest available measurements to estimate the $H\alpha$ emission and X-ray flux levels at the times of the *HST* observations (summarized in Table 4). All four *HST* observations occurred when the $H\alpha$ emission was weak and the soft X-ray flux was uniformly strong.

The other important optical emission line in the spectrum of HD 226868 is the He II $\lambda 4686$ feature. Gies & Bolton (1986b) and Ninkov et al. (1987) found that this emission probably forms between the supergiant and black hole in a higher density and slower region of the wind, the focused wind predicted by Friend & Castor (1982). We obtained a limited number of spectra of the He II $\lambda 4686$ feature (runs 8 and 9 in Table 1) at the times of the

¹⁴<http://xte.mit.edu/>

two *HST* observation sets, and these observations show profile variations with orbital phase that are quite similar to those seen previously (Gies & Bolton 1986b; Ninkov et al. 1987; Karitskaya et al. 2006b). We present in Table 5 the observed equivalent width of the He II $\lambda 4686$ emission/absorption complex (made by numerical integration between 4677 and 4695 Å) for spectra from these two runs and from a third run (#10 in Table 1) that occurred when the system had returned to the X-ray low/hard state. There was no significant difference in the amount of He II $\lambda 4686$ emission present between the times of the two X-ray states. We compare in Table 6 the averages of these measurements with earlier orbital phase averages (Gies & Bolton 1986a; Brocksopp et al. 1999) and time averages (Ninkov et al. 1987) of the emission strength that correspond mainly to times when the system was in the low/hard X-ray state. Note that Ninkov et al. (1987) report only the net emission equivalent width after subtraction of the photospheric absorption profile of the similar star HD 149038, and we estimate that this procedure increased the emission strength by 0.25\AA according to the plot of the spectrum of HD 149038 given in Figure 1 of Ninkov et al. (1987). We find that the He II $\lambda 4686$ emission has remained more or less constant in strength over the decades of observation and between the X-ray states, and this suggests the tidal gas stream towards the black hole experiences much less variation than does the global wind as observed in the H α emission line.

4. Orbital Variations in the UV Wind Lines

Our primary interest here is how the X-ray flux ionizes portions of the supergiant’s wind and how our line of sight through the ionized zones changes with orbital phase. We show in Figures 5, 6, and 7 the changes observed between conjunctions in the major UV wind lines of N V $\lambda\lambda 1238, 1242$, Si IV $\lambda\lambda 1393, 1402$, and C IV $\lambda\lambda 1548, 1550$. In a companion paper, Vrtilik et al. (2008) show the variations observed in several other weaker lines. The top panel in each of these figures shows the variations in 2002 between the phases with the black hole behind ($\phi = 0.0$; *solid line*) and in the foreground of the supergiant ($\phi = 0.5$; *dotted line*), and the bottom panel shows the same for the 2003 run. The spectra are plotted as a function of radial velocity for the shorter wavelength component in the frame of the supergiant (according to the orbital solution in Table 3). All three of these transitions display a large reduction in the extent and depth of the blueshifted absorption component when the black hole is in the foreground (the Hatchett-McCray effect). These changes reflect the X-ray photoionization and resulting superionization of these ions in the wind gas seen projected against the supergiant. We also find some evidence of the associated reduction in the strength of the red emission component due to the loss of these gas ions in the outflow away from our line of sight when the black hole is in the background. The variations between

conjunctions appear to be almost identical for the observations in 2002 and 2003, which is probably due to the very similar X-ray fluxes that existed at those times of observation (§3, Table 4).

The shapes of the wind profiles near orbital phase $\phi = 0.5$ suggest that the P Cygni absorption troughs have almost entirely disappeared, or that the wind ionization extends all the way towards the exposed photosphere of the supergiant. We made some simple calculations of the appearance of wind profiles that arise only from the gas hidden from the X-ray source, the so-called shadow wind (Blondin 1994) that is illustrated diagrammatically in Figure 8. Here we assume that the normal supergiant wind is confined to the region where the line of sight to the black hole is blocked by the supergiant. However, we expect that in reality this shadow region is partially exposed to X-rays by wind scattering (probably comparable to the scattering along our line of sight through the wind, i.e., a few percent of the unobscured X-ray flux; Wen et al. 1999) and by the Coriolis deflection that will bring the shadowed gas into regions of X-ray illumination (Blondin 1994). The line synthesis calculations are based on a modification of the Sobolev-Exact Integration method (Lamers, Cerruti-Sola, & Perinotto 1987) that was developed by van Loon et al. (2001). The simplifying assumption in this model is that the observer lies along the axis joining the stars at the two conjunctions (or that the orbital inclination is $i = 90^\circ$ and the orbital phases are $\phi = 0.0, 0.5$). However, since the actual inclination is smaller ($i = 33^\circ - 40^\circ$; Gies & Bolton 1986a; Brocksopp, Fender, & Pooley 2002), our line of sight at the conjunctions will include somewhat different portions of the occulted and unocculted wind (Fig. 8), so these models are first approximations of the predicted variations for a shadow wind. In a companion paper (Vrtilek et al. 2008), we present a more complete calculation based upon a realistic orbital inclination and the method outlined by Boroson et al. (1999).

The line synthesis is based upon a set of adopted parameters and two fitting parameters. Most of the adopted parameters come from the study of Cyg X-1 and similar X-ray binaries by van Loon et al. (2001), and in particular, we assume a wind velocity law exponent of $\gamma = 1$ (eq. 2 in van Loon et al. 2001), a semimajor axis equivalent to $2.1R_\star$ (where R_\star is the radius of the supergiant; Gies & Bolton 1986a), and a characteristic turbulent velocity in the wind equal to $0.1v_\infty$ (Groenewegen, Lamers, & Pauldrach 1989) where v_∞ is the terminal velocity in the undisturbed wind. The photospheric components corresponding to the wind transitions were assumed to be Gaussian in shape with parameters set by Gaussian fits of the photospheric profiles in the non-LTE, line blanketed model spectra of Lanz & Hubeny (2003) (for $T_{\text{eff}} = 30000$ K, $\log g = 3.0$, $V \sin i = 100$ km s $^{-1}$, a linear limb darkening coefficient of $\epsilon = 0.50$, and a spectral resolving power of 10000).

The final two parameters, the wind terminal velocity v_∞ and the integrated optical

depth through the shadow wind of the blue component of the transition τ , were fit by trial and error in order to match the entire set of the three wind lines at each conjunction. Note that the value of v_∞ is set mainly by fits of the profiles at orbital phase $\phi = 0.0$ when the undisturbed wind is in the foreground and projected against the star. The best match was made with $v_\infty = 1200 \text{ km s}^{-1}$ and $\tau = 6, 4,$ and 10 for the N V, Si IV, C IV features, respectively. The shadow wind model profiles are presented in Figures 9, 10, and 11 for these three wind lines. The top panel in these figures shows the model (*diamonds*) and average observed spectra (*solid line*) for $\phi = 0.0$ while the lower panel illustrates the same for phase $\phi = 0.5$ (black hole in the foreground). The model profiles were renormalized in flux in each case to match the pseudo-continuum beyond the line wings in the observed spectra. Each panel also contains the predicted photospheric spectrum for the region from the models of Lanz & Hubeny (2003). These representative fits successfully reproduce many of the profile characteristics, especially when line blending from the other photospheric lines is taken into account. This suggests that the geometry of the photoionization zone is probably not too different from that assumed for a shadow wind (at least for the high/soft X-ray state). However, we caution again that our fitting parameters are based upon an axial viewing orientation while our actual view is more oblique. For example, according to the geometry sketched in Figure 8 (for $i = 40^\circ$), the fastest moving part of the shadow wind that is projected against the supergiant at $\phi = 0.0$ occurs at a radial distance from the center of the supergiant of $\approx 4.6R_\star$ where the wind has not yet reached terminal velocity. Thus, our fit value of $v_\infty = 1200 \text{ km s}^{-1}$ is probably well below the actual value (which is probably closer to 1600 km s^{-1}).

The low orbital inclination and the subsequent limited projection of the shadow wind region against the disk of the photosphere results in P Cygni absorption troughs that are unusually weak for the spectra of supergiants like HD 226868. We show in Figures 12 and 13 montages of the Si IV and C IV wind features in four other O9.7 Iab supergiants as seen in high dispersion spectra from the *IUE* archive. The mean spectrum of HD 226868 at orbital phase $\phi = 0.0$ (shown at the top of both figures) shows that the wind profiles have a lower optical depth and attain a smaller blue-shifted velocity because only a small portion of the shadow wind is projected against the disk of the supergiant at its inferior conjunction (see Fig. 8).

5. Comparison of the Wind Lines in the X-ray Low and High States

Our original goal was to obtain another set of STIS spectra when Cyg X-1 was in the low/hard X-ray state in order to determine how the wind ionization conditions change with

X-ray state. With the loss of STIS, such a comparison is not possible at present. However, the low dispersion FUV spectra of HD 226868 made with *IUE* were in most cases made when Cyg X-1 was in the low/hard state. Thus, we can investigate differences in the wind ionization properties between X-ray states through a comparison of the *HST* high/soft state spectra with the *IUE* low/hard state spectra.

We collected 30, low dispersion, short wavelength prime camera spectra of HD 226868 from the *IUE* archive, and transformed these to rectified flux versions on a uniform wavelength grid. Next, we smoothed, rectified, and rebinned the *HST* STIS spectra onto the same *IUE* wavelength grid so that the line blended structures would appear the same as they do in the *IUE* spectra. We then measured the effective absorption strength by determining the mean flux across a spectral range that extends over the full range of the apparent wind feature (as done by van Loon et al. 2001). This average flux will reflect both the changing P Cygni absorption and the other line blends (including interstellar components), but since the latter are generally constant in time, the average flux will serve to show the relative variations in the wind absorption (low flux when the P Cygni trough is deep and high flux when the trough weakens).

The average flux measurements for both the *IUE* and rebinned *HST* spectra are given in Table 7, which lists the heliocentric Julian date of mid-exposure, orbital phase (from Table 3), the mean rectified flux across the Si IV and C IV wind lines, the telescope of origin, the X-ray state at the time of the observations, and a code for references discussing the contemporary X-ray fluxes. Note that we did not measure the N V transition in the *IUE* spectra because these spectra are poorly exposed at the short wavelength end. The *IUE* average flux measurements have a typical error of $\pm 7\%$ based upon the scatter in the results from closely separated pairs of spectra.

The average fluxes across the wind lines are plotted as a function of orbital phase in Figures 14 and 15 for Si IV and C IV, respectively (see a similar depiction in Fig. 1 from van Loon et al. 2001). Different symbols show these measurements for the different X-ray states as observed with *IUE* and *HST*. We suspect that despite our efforts to rectify the *IUE* and *HST* spectra in the same way, there are probably still some systematic differences since the mean fluxes for the *HST* spectra appear to be somewhat lower than those for the *IUE* spectra. Nevertheless, the amplitude of line strength variation appears to be more or less the same in each of the *IUE* low/hard state, *IUE* high/soft state, and *HST* high/soft state spectra. This result indicates that the Hatchett-McCray effect (and the amount of wind photoionization it represents) occurs at about the same level in both X-ray states.

6. Discussion

The X-ray accretion flux of Cyg X-1 is fueled by mass transfer from the supergiant. We argue in this section that the mass transfer process is dominated by a wind focused along the axis joining the stars. However, the accretion of this gas by the black hole may be influenced by the strength of the radiatively driven shadow wind that is directed away from the black hole. We begin by reviewing the most pertinent observational results from this investigation, and then we consider the interplay between the dynamics of the wind outflow and the X-ray accretion flux.

First, the *HST* STIS spectra of HD 226868 that we obtained at two epochs when the system was in the high/soft state show dramatic variations in the wind line strength that result from a superionization of the gas atoms illuminated by the X-ray flux. Shadow wind models, in which the wind ions only exist in the region where X-rays are blocked by the supergiant, make a reasonably good match to the observed profile variations, so we suspect that X-ray photoionization dominates much of the zone between the black hole and the facing hemisphere of the supergiant. A similar degree of wind ionization probably also exists in the X-ray low/hard state since similar orbital variations in wind line strength are found in *IUE* low dispersion spectra made during the X-ray low/hard state.

Second, the *HST* spectra suggest that stellar wind gas emanating from parts of the photosphere facing the X-ray source attains only a small velocity before becoming photoionized. For example, the highest optical depth wind feature, C IV $\lambda\lambda 1548, 1550$, shows only a very modest P Cygni absorption core at phase $\phi = 0.5$ (see Fig. 11) that extends blueward no more than about -400 km s^{-1} (and it is possible that this small component results from a minor part of shadow wind projected against supergiant at $\phi = 0.5$; see Fig. 8). This very low wind speed is probably less than the stellar escape velocity ($\sim 700 \text{ km s}^{-1}$ near the poles).

These results from the UV wind lines indicate that very little mass loss is occurring by a radiatively driven wind for surface regions that are exposed to the X-ray source. The fact that the wind features appear similarly weak in *IUE* spectra obtained in the low/hard state suggests that a spherical, radiatively driven wind from the hemisphere of the supergiant facing the black hole is probably always weak or absent, and thus, accretion from a spherically symmetric wind must play a minor role in feeding the black hole in Cyg X-1.

On the other hand, we found that the emission equivalent width of the He II $\lambda 4686$ line is consistently strong between X-ray states and over the available record of observation. The orbital phase variations of this spectral feature (Gies & Bolton 1986b; Ninkov et al. 1987) are successfully matched by models of emission from an enhanced density and slower gas outflow

region between the stars that is expected for a focused stellar wind (Friend & Castor 1982). Thus, while X-ray ionization reduces the wind outflow away from the axis joining the stars, the X-ray flux is apparently insufficient to stop the outflow in the denser gas of the focused wind (the result of both tidal and radiative forces). Consequently, it is this focused wind component that is probably the primary means of mass transfer in Cyg X-1. We caution that the relative constancy of the He II $\lambda 4686$ emission flux does not necessarily imply that the mass loss rate in the focused wind is also steady. For example, the increased X-ray photoionization during the high/soft state may lead to an increase in He II $\lambda 4686$ emission (see Fig. 2 in Gies & Bolton 1986b), so that a lower mass loss rate but higher ionization fraction might result in the same amount of observed emission. However, the presence of the He II $\lambda 4686$ emission in both X-ray states indicates that focused wind mass loss always occurs at some level.

Finally, we confirm that the H α P Cygni line forms mainly in the base of the stellar wind of the supergiant since we observe that H α follows the orbital velocity curve of the supergiant (Fig. 1). The new observations are consistent with earlier results (Gies et al. 2003; Tarasov et al. 2003) in demonstrating that the H α emission strength is generally weaker in the high/soft X-ray state. Photoionization and heating may extend down to atmospheric levels where the gas densities are sufficient to create H α emission, so that the reduction in H α strength in the X-ray high/soft state may partially result from photoionization related processes. However, Gies et al. (2003) showed that H α emission variability was present in those Doppler shifted parts of the profile corresponding to the X-ray shadow hemisphere of the supergiant (see their Fig. 15), so part of the H α variations must be related to gas density variations at the base of the stellar wind. Thus, the observed H α variations suggest that the high/soft X-ray state occurs when the global, radiatively driven part of the wind is weaker. Long term, quasi-cyclic variations in wind strength are apparently common among hot supergiants (Markova et al. 2005).

Gies et al. (2003) and Tarasov et al. (2003) suggested that the variations in X-ray state are caused by changes in wind velocity due to changes in supergiant mass loss rate. During times when the supergiant’s wind is denser and the mass loss rate is higher, the photoionization region would be more restricted to the region closer to the black hole. Consequently, a radiatively driven wind could accelerate to a higher speed before stalling when the gas enters the ionization zone, and thus, the faster wind would result in a lower black hole accretion rate and X-ray luminosity (creating the low/hard X-ray state). Conversely, if the wind mass loss rate drops, then the X-ray ionization zone will expand, the maximum wind velocity towards the black hole will decline, and the net accretion rate will increase (perhaps creating the high/soft state; Ho & Arons 1987). This creates a positive feedback mechanism that may continue until the wind is ionized all the way down to the stellar photosphere facing

the X-ray source (Day & Stevens 1993; Blondin 1994).

If this scenario is correct, then we expect that the outflow velocities in the direction of the black hole (as measured in blue extent of the P Cygni lines at phase $\phi = 0.5$) will be larger than the supergiant escape velocity during the X-ray low/hard state. The superb quality *HST*/STIS spectra indicate that outflow velocities are too low to launch the wind during the X-ray high/soft state. Moreover, the low resolution *IUE* spectra from the low/hard state appear to show a very similar pattern of the loss of the P Cygni absorption at $\phi = 0.5$ (Fig. 12 and 13), indicating that significant ionization zones still exist in the low/hard state. Taken at face value, these *IUE* results suggest that the spherical component of wind outflow towards the black hole is weak and slow in both X-ray states, so a wind speed modulation is probably not the explanation for the accretion variations associated with the X-ray states. We will require new, high quality, UV spectroscopy of Cyg X-1 during the low/hard state in order to make a definitive test of this idea.

The radiatively driven wind of the supergiant leads to effective mass loss only in the X-ray shadowed hemisphere and in the focused wind between the stars in Cyg X-1. The outflow in the shadow wind region will experience a Coriolis deflection, so that the trailing regions of the shadow wind will eventually enter the zone of X-ray illumination (Blondin 1994). Once photoionized, this gas will stall with the loss of the important ions for radiative acceleration, and some of this slower gas may extend around the orbital plane to the vicinity of the black hole. Although this deflected wind gas is probably not a major accretion source (Blondin 1994), it may affect the accretion dynamics of the focused wind. For example, when the shadow wind mass loss rate is high (times of strong $H\alpha$ emission), the resulting stalled wind component will create a higher ambient gas density on the leading side of the zone surrounding the black hole. The focused wind flow will make a trajectory towards the following side of the black hole, and while gas passing closer to the black hole will merge into an accretion disk, gas further out will tend to move past the black hole before turning into the outskirts of the disk. The presence of the stalled gas on the leading side may deflect away this outer, lower density part of the flow and effectively inhibit gas accretion from the focused wind. The subsequent reduction in gas accretion by the black hole may correspond to the conditions required to produce the low/hard X-ray state, while conversely a reduction in the stalled gas from the shadow wind may promote mass accretion and produce the high/soft state (Brocksopp et al. 1999; Done 2002; McClintock & Remillard 2006). Clearly, new hydrodynamical simulations are needed to test whether the stalled wind component is sufficient to alter the accretion of gas from the focused wind and create the environments needed for the X-ray transitions.

We thank the staffs of the David Dunlap Observatory, Kitt Peak National Observa-

tory, Dominion Astrophysical Observatory, Ondřejov Observatory, and the Space Telescope Science Institute (STScI) for their support in obtaining these observations. The KPNO spectra supporting the second *HST* run were obtained with the assistance of participants in the NOAO Teacher Leaders in Research Based Science Education program, including Joan Kadaras (Westford Academy, Westford, MA), Steve Harness (Kingsburg Joint Union High School, Kingsburg, CA), Elba Sepulveda (CROEM, Mayaguez, PR), and Dwight Taylor (Goldenvue Middle School, Anchorage, AK). We also thank Saku Vrtilek and Bram Boroson for helpful comments, and we are especially grateful to an anonymous referee whose report was pivotal to our discussion of the results. Support for *HST* proposal number GO-9840 was provided by NASA through a grant from the Space Telescope Science Institute, which is operated by the Association of Universities for Research in Astronomy, Incorporated, under NASA contract NAS5-26555. The X-ray results were provided by the ASM/RXTE teams at MIT and at the RXTE SOF and GOF at NASA's GSFC. The *IUE* data presented in this paper were obtained from the Multimission Archive at the Space Telescope Science Institute (MAST). Support for MAST for non-HST data is provided by the NASA Office of Space Science via grant NAG5-7584 and by other grants and contracts. Bolton's research is partially supported by a Natural Sciences and Engineering Research Council of Canada (NSERC) Discovery Grant. Hadrava's research is funded under grant projects GAČR 202/06/0041 and LC06014. Herrero thanks the Spanish MEC for support under project AYA 2007-67456-C02-01. This work was also supported by the National Science Foundation under grants AST-0205297, AST-0506573, and AST-0606861. Institutional support has been provided from the GSU College of Arts and Sciences and from the Research Program Enhancement fund of the Board of Regents of the University System of Georgia, administered through the GSU Office of the Vice President for Research. We are grateful for all this support.

REFERENCES

- Blondin, J. M. 1994, *ApJ*, 435, 756
- Blondin, J. M., Kallman, T. R., Fryxell, B. A., & Taam, R. E. 1990, *ApJ*, 356, 591
- Boroson, B., Kallman, T., McCray, R., Vrtilek, S. D., & Raymond, J. 1999, *ApJ*, 519, 191
- Brocksopp, C., Fender, R. P., Larionov, V., Lyuty, V. M., Tarasov, A. E., Pooley, G. G., Paciesas, W. S., & Roche, P. 1999, *MNRAS*, 309, 1063
- Brocksopp, C., Fender, R. P., & Pooley, G. G. 2002, *MNRAS*, 336, 699
- Davis, R., & Hartmann, L. 1983, *ApJ*, 270, 671

- Day, C. S. R., & Stevens, I. R. 1993, *ApJ*, 403, 322
- Done, C. 2002, *Roy. Soc. London Phil. Tr. A*, 360, Issue 1798, 1967
- Friend, D. B., & Castor, J. I. 1982, *ApJ*, 261, 293
- Gallo, E., Fender, R., Kaiser, C., Russell, D., Morganti, R., Oosterloo, T., & Heinz, S. 2005, *Nature*, 436, 819
- Gies, D. R., & Bolton, C. T. 1986a, *ApJ*, 304, 371
- Gies, D. R., & Bolton, C. T. 1986b, *ApJ*, 304, 389
- Gies, D. R., et al. 2003, *ApJ*, 583, 424
- Groenewegen, M. A. T., Lamers, H. J. G. L. M., & Pauldrach, A. W. A. 1989, *A&A*, 221, 78
- Hadrava, P. 2007, *Proceedings of RAGtime 8/9: Workshops on black holes and neutron stars*, ed. S. Hledik & Z. Stuchlik (Opava, Czech Republic: Silesian Univ.), 73 (arXiv:0710.0758v1)
- Hatchett, S., & McCray, R. 1977, *ApJ*, 211, 552
- Herrero, A., Kudritzki, R. P., Gabler, R., Vilchez, J. M., & Gabler, A. 1995, *A&A*, 297, 556
- Ho, C., & Arons, J. 1987, *ApJ*, 316, 283
- Kaper, L. 1998, in *Boulder-Munich II: Properties of Hot, Luminous Stars* (ASP Conf. Series, Vol. 131), ed. I. D. Howarth (San Francisco: ASP), 427
- Karitskaya, E. A., et al. 2006a, *IBVS*, 5678, 1
- Karitskaya, E. A., et al. 2006b, *Astron. & Ap. Trans.*, 24, 383
- Kemp, J. C., Barbour, M. S., & McBirney, R. E. 1981, *ApJ*, 244, L73
- Lamers, H. J. G. L. M., Cerruti-Sola, M., & Perinotto, M. 1987, *ApJ*, 314, 726
- Lanz, T., & Hubeny, I. 2003, *ApJS*, 146, 417
- Levine, A. M., Bradt, H., Cui, W., Jernigan, J. G., Morgan, E. H., Remillard, R., Shirey, R. E., & Smith, D. A. 1996, *ApJ*, 469, L33
- Ling, J. C., Mahoney, W. A., Wheaton, W. A., Jacobson, A. S., & Kaluzienski, L. 1983, *ApJ*, 275, 307

- Markova, N., Puls, J., Scuderi, S., & Markov, H. 2005, *A&A*, 440, 1133
- McClintock, J. E., & Remillard, R. A. 2006, in *Compact Stellar X-ray Sources*, ed. W. H. G. Lewin & M. van der Klis (Cambridge, UK: Cambridge Univ. Press), 157
- McConnell, M. L., et al. 2002, *ApJ*, 572, 984
- Miller, J. M., Wojdowski, P., Schulz, N. S., Marshall, H. L., Fabian, A. C., Remillard, R. A., Wijnands, R., & Lewin, W. H. G. 2005, *ApJ*, 620, 398
- Morbey, C. L., & Brosterhus, E. B. 1974, *PASP*, 86, 455
- Ninkov, Z., Walker, G. A. H., & Yang, S. 1987, *ApJ*, 321, 438
- Oda, M. 1980, *IAU Circ.*, 3502, 2
- Ogawara, Y., Mitsuda, K., Masai, K., Vallergera, J. V., Cominsky, L. R., Grunsfeld, J. M., Kruper, J. S., & Ricker, G. R. 1982, *Nature*, 295, 675
- Penny, L. R., Gies, D. R., & Bagnuolo, W. G., Jr. 1999, *ApJ*, 518, 450
- Perotti, F., et al. 1986, *ApJ*, 300, 297
- Priedhorsky, W. C., Terrell, J., & Holt, S. S. 1983, *ApJ*, 270, 233
- Puls, J., et al. 1996, *A&A*, 305, 171
- Shaposhnikov, N., & Titarchuk, L. 2006, *ApJ*, 643, 1098
- Stevens, I. R. 1991, *ApJ*, 379, 310
- Tarasov, A. E., Brocksopp, C., & Lyuty, V. M. 2003, *A&A*, 402, 237
- Treves, A., et al. 1980, *ApJ*, 242, 1114
- van Loon, J. Th., Kaper, L., & Hammerschlag-Hensberge, G. 2001, *A&A*, 375, 498
- Vrtilek, S. D., Boroson, B. S., Hunacek, A., Gies, D., & Bolton, C. T. 2008, *ApJ*, in press
- Walborn, N. R. 1973, *ApJ*, 179, L123
- Wen, L., Cui, W., Levine, A. M., & Bradt, H. V. 1999, *ApJ*, 525, 968
- Wilms, J., Nowak, M. A., Pottschmidt, K., Pooley, G. G., & Fritz, S. 2006, *A&A*, 447, 245

Table 1. Journal of Spectroscopy

Run Number	Dates (HJD-2,450,000)	Range (Å)	Resolving Power ($\lambda/\Delta\lambda$)	N	Observatory/Telescope/Spec., Grating/Detector
1	2419.8 – 2828.7	6510 – 6710	8900	70	DDO/1.88m/Cass., 1800 g mm ⁻¹ /Thomson 1024 × 1024
2	2448.7 – 2453.9	6530 – 6710	7400	15	KPNO/0.9m/Coudé, B (order 2)/TI5
3	2825.8 – 2828.9	6320 – 8970	2720	6	KPNO/0.9m/Coudé, RC400 (order 1)/F3KB
4	2826.8 – 2827.9	6353 – 6756	6900	10	DAO/1.85m/Cass., 21121R/SITe-2
5	2730.7 – 2904.5	6258 – 6770	10900	24	Ondřejov/2m/Coudé, 700mm/SITe 2000 × 800
6	2450.3 – 2453.3	1150 – 1740	14500	4	HST/2.4m/STIS, G140M/FUV-MAMA
7	2825.7 – 2827.8	1150 – 1740	14500	4	HST/2.4m/STIS, G140M/FUV-MAMA
8	2448.7 – 2454.0	4624 – 4740	13000	14	KPNO/0.9m/Coudé, B (order 3)/TI5
9	2824.9 – 2826.8	3759 – 5086	2990	3	KPNO/0.9m/Coudé, RC400 (order 2)/F3KB
10	2912.8 – 2915.8	4182 – 4942	5700	5	KPNO/4m/RC Spec., BL380 (order 2)/T2KB

Table 2. Radial Velocity and H α Equivalent Width Measurements

HJD (-2,450,000)	Orbital Phase	V_r (km s $^{-1}$)	ΔV_r (km s $^{-1}$)	($O - C$) (km s $^{-1}$)	W_λ (H α) (\AA)	Run Number
2419.847 ...	0.115	45.4	3.1	2.2	-0.38	1
2426.848 ...	0.365	55.6	4.5	6.1	-0.54	1
2427.841 ...	0.543	-22.9	3.2	1.6	-0.75	1
2429.605 ...	0.858	-65.3	3.1	-3.3	-0.02	1
2443.803 ...	0.393	42.4	3.2	2.1	-0.10	1
2445.846 ...	0.758	-88.6	3.1	-10.6	-0.07	1
2446.804 ...	0.929	-42.0	3.1	-5.4	-0.10	1
2448.694 ...	0.267	68.4	1.3	1.0	0.01	2
2448.850 ...	0.294	67.5	3.1	2.5	0.10	1
2448.954 ...	0.313	66.5	1.1	4.3	-0.22	2
2449.683 ...	0.443	18.2	1.8	-2.2	-0.04	2
2449.790 ...	0.462	7.7	3.3	-4.3	-0.15	2
2449.932 ...	0.488	-8.9	1.7	-9.5	-0.48	2
2450.272 ...	0.548	-27.5	3.0	-0.6	...	6
2450.335 ...	0.560	-31.6	3.0	0.2	...	6
2450.637 ...	0.614	-45.7	3.2	7.2	-0.43	1
2450.667 ...	0.619	-49.2	1.8	5.5	-0.60	2
2450.715 ...	0.628	-60.3	3.5	-2.8	-0.56	1
2450.760 ...	0.636	-60.2	1.3	-0.2	-0.72	2
2450.792 ...	0.641	-53.6	3.1	8.1	-0.38	1
2450.812 ...	0.645	-66.3	3.1	-3.6	-0.83	1
2450.912 ...	0.663	-66.6	1.6	0.8	-0.74	2
2451.603 ...	0.786	-79.6	3.1	-3.4	-0.69	1
2451.642 ...	0.793	-82.9	3.1	-7.4	-0.33	1
2451.642 ...	0.793	-82.3	3.1	-6.9	-0.35	1
2451.686 ...	0.801	-76.8	3.2	-2.5	-0.54	1
2451.701 ...	0.803	-77.0	1.6	-3.0	-0.45	2
2451.709 ...	0.805	-79.7	3.2	-6.0	-0.73	1
2451.737 ...	0.810	-76.0	3.1	-3.1	-0.41	1
2452.711 ...	0.984	-12.9	3.1	-0.4	0.11	1
2452.733 ...	0.988	-10.9	3.1	-0.2	-0.04	1
2452.734 ...	0.988	-9.1	1.6	1.4	0.04	2
2452.772 ...	0.995	-5.5	3.2	2.0	0.13	1
2452.795 ...	0.999	-5.3	3.2	0.3	-0.34	1
2452.836 ...	0.006	-1.2	1.3	1.1	0.16	2
2452.962 ...	0.029	12.4	1.6	4.4	0.10	2
2453.210 ...	0.073	34.0	3.0	6.9	...	6
2453.272 ...	0.084	34.5	3.0	2.8	...	6
2453.664 ...	0.154	59.2	1.5	4.2	-0.21	2
2453.744 ...	0.168	57.4	3.1	-1.1	-0.23	1
2453.754 ...	0.170	56.7	1.2	-2.1	-0.22	2
2453.766 ...	0.172	53.3	3.1	-6.0	-0.22	1
2453.806 ...	0.180	64.5	3.2	3.7	-0.18	1
2453.828 ...	0.183	59.8	3.1	-1.8	-0.13	1
2453.845 ...	0.186	53.1	3.1	-9.0	-0.66	1

Table 2—Continued

HJD (-2,450,000)	Orbital Phase	V_r (km s ⁻¹)	ΔV_r (km s ⁻¹)	($O - C$) (km s ⁻¹)	$W_\lambda(\text{H}\alpha)$ (Å)	Run Number
2453.934 ...	0.202	59.9	1.3	-4.7	-0.09	2
2454.635 ...	0.327	57.3	3.1	-2.1	-0.09	1
2454.660 ...	0.332	52.6	3.1	-5.8	0.09	1
2454.682 ...	0.336	53.4	3.1	-4.0	0.12	1
2454.705 ...	0.340	49.5	3.1	-7.0	-0.07	1
2454.728 ...	0.344	44.7	3.1	-10.8	-0.05	1
2454.750 ...	0.348	44.8	3.1	-9.6	-0.17	1
2454.773 ...	0.352	43.5	3.1	-9.8	-0.22	1
2454.796 ...	0.356	39.6	3.1	-12.6	-0.07	1
2454.818 ...	0.360	41.2	3.1	-9.9	-0.04	1
2454.841 ...	0.364	43.6	3.1	-6.2	-0.03	1
2454.859 ...	0.368	44.2	3.1	-4.6	-0.55	1
2463.626 ...	0.933	-43.2	3.2	-8.3	-0.15	1
2479.857 ...	0.832	-64.9	3.1	3.8	-0.13	1
2519.667 ...	0.941	-31.2	3.1	0.5	-0.30	1
2524.692 ...	0.838	-70.8	3.1	-3.6	-0.28	1
2530.586 ...	0.891	-47.5	3.1	3.9	-0.13	1
2554.578 ...	0.175	63.8	3.1	3.9	-0.08	1
2571.581 ...	0.211	65.1	3.1	-0.6	-0.77	1
2576.659 ...	0.118	47.9	3.1	3.8	-0.29	1
2578.510 ...	0.449	12.8	3.1	-5.1	-0.39	1
2580.562 ...	0.815	-70.5	3.1	1.6	-0.73	1
2592.565 ...	0.959	-29.0	3.1	-5.1	-1.05	1
2611.473 ...	0.335	57.2	3.1	-0.5	-0.57	1
2613.498 ...	0.697	-78.6	3.1	-4.5	-0.83	1
2619.458 ...	0.761	-79.6	3.1	-1.7	-0.85	1
2625.476 ...	0.836	-75.7	3.3	-8.0	-0.90	1
2626.457 ...	0.011	-4.5	3.1	-4.4	-0.57	1
2638.476 ...	0.157	60.8	3.1	5.0	-0.60	1
2646.474 ...	0.585	-31.6	3.1	10.8	-1.05	1
2709.867 ...	0.906	-44.6	3.3	1.2	-0.70	1
2730.654 ...	0.618	-40.0	5.0	14.4	-1.21	5
2730.755 ...	0.636	-64.4	4.2	-4.2	-1.82	1
2744.818 ...	0.148	56.7	3.1	3.4	-1.25	1
2746.612 ...	0.468	14.6	3.0	5.2	-1.34	5
2762.871 ...	0.371	48.3	3.1	0.7	-0.64	1
2805.784 ...	0.035	2.3	3.1	-8.3	-0.35	1
2813.681 ...	0.445	18.4	3.1	-1.2	-0.53	1
2824.647 ...	0.403	-0.29	1
2825.702 ...	0.592	-31.8	3.0	13.0	...	7
2825.765 ...	0.603	-41.1	3.0	7.9	...	7
2825.839 ...	0.616	-44.3	4.6	9.4	-0.40	3
2825.844 ...	0.617	-43.3	10.7	10.7	-0.36	3
2826.817 ...	0.791	-65.7	3.1	10.1	-0.34	1
2826.832 ...	0.793	-49.9	8.0	25.5	-0.44	4

Table 2—Continued

HJD (-2,450,000)	Orbital Phase	V_r (km s ⁻¹)	ΔV_r (km s ⁻¹)	$(O - C)$ (km s ⁻¹)	$W_\lambda(\text{H}\alpha)$ (Å)	Run Number
2826.860 ...	0.798	-69.2	5.4	5.6	-0.29	4
2826.885 ...	0.803	-69.4	5.2	4.7	-0.36	4
2826.909 ...	0.807	-67.3	5.4	6.2	-0.37	4
2826.933 ...	0.811	-62.6	5.2	10.1	-0.43	4
2827.702 ...	0.949	-27.9	3.0	0.3	...	7
2827.765 ...	0.960	-26.4	3.0	-3.0	...	7
2827.800 ...	0.966	-23.7	6.8	-3.2	-0.44	3
2827.812 ...	0.968	-23.7	7.2	-4.1	-0.47	3
2827.812 ...	0.968	-23.0	5.2	-3.5	-0.60	4
2827.836 ...	0.973	-21.7	5.2	-4.1	-0.55	4
2827.882 ...	0.981	-13.5	5.3	0.4	-0.68	4
2827.905 ...	0.985	-14.0	5.2	-2.0	-0.60	4
2827.929 ...	0.989	-7.3	5.2	2.8	-0.79	4
2828.594 ...	0.108	40.7	3.1	0.1	-0.16	1
2828.657 ...	0.119	45.3	3.1	0.7	0.08	1
2828.680 ...	0.123	45.6	3.1	-0.3	-0.09	1
2828.702 ...	0.127	46.4	3.1	-0.8	-0.04	1
2828.725 ...	0.131	45.4	3.1	-3.0	-0.13	1
2828.747 ...	0.135	50.0	3.1	0.3	-0.03	1
2828.885 ...	0.160	57.5	5.5	1.1	-0.20	3
2828.892 ...	0.161	55.5	4.6	-1.3	-0.17	3
2835.440 ...	0.330	61.4	2.9	2.7	0.00	5
2840.510 ...	0.236	-0.09	5
2846.494 ...	0.305	64.8	2.9	1.2	-0.53	5
2857.443 ...	0.260	71.3	2.9	3.6	-0.09	5
2857.471 ...	0.265	69.7	2.9	2.1	-0.24	5
2859.510 ...	0.629	-72.4	2.9	-14.4	-0.52	5
2860.535 ...	0.812	-72.9	2.9	-0.2	-0.48	5
2860.558 ...	0.816	-71.8	2.9	0.1	-0.47	5
2861.539 ...	0.991	-7.9	2.9	1.3	-0.31	5
2862.547 ...	0.171	61.6	3.2	2.5	-0.35	5
2862.572 ...	0.176	58.2	2.9	-1.8	-0.35	5
2874.472 ...	0.301	72.1	2.9	7.9	-0.82	5
2874.494 ...	0.305	67.6	2.9	4.1	-0.76	5
2874.516 ...	0.309	72.6	2.9	9.6	-0.70	5
2874.538 ...	0.312	70.5	2.9	8.2	-0.66	5
2878.417 ...	0.005	5.0	2.9	7.7	-0.68	5
2878.441 ...	0.009	8.2	2.9	9.0	-0.54	5
2898.466 ...	0.585	-36.2	2.9	6.2	-1.14	5
2901.357 ...	0.102	38.4	3.1	0.0	-1.26	5
2903.436 ...	0.473	22.2	2.9	14.9	-0.96	5
2903.475 ...	0.480	16.9	2.9	12.9	-0.98	5
2904.480 ...	0.659	-55.5	2.9	11.1	-1.12	5

Table 3. Circular Orbital Elements

Element	Brocksopp et al. (1999)	Gies et al. (2003)	This Work
P (d)	5.599829 (16)	5.599829 ^a	5.599829 ^a
$T(\text{IC})$ (HJD-2,400,000)	41,874.707 (9)	51,730.449 (8)	52,872.788 (9)
K_1 (km s ⁻¹)	74.9 (6)	75.6 (7)	73.0 (7)
V_0 (km s ⁻¹)	-7.0 (5)	-5.1 (5)
σ (km s ⁻¹)	5.3	5.4

^aFixed.

Note. — Numbers in parentheses give the error in the last digit quoted.

Table 4. H α Equivalent Widths and X-ray Flux Counts for the *HST* Observation Times

HJD (-2,450,000)	Orbital Phase	$W_\lambda(\text{H}\alpha)$ (\AA)	Flux (1.5 – 3 keV) (ASM counts)
2450.3.....	0.55	-0.45 (15)	52 (10)
2453.2.....	0.08	-0.02 (10)	60 (10)
2825.7.....	0.60	-0.39 (10)	50 (10)
2827.7.....	0.95	-0.44 (10)	42 (10)

Note. — Numbers in parentheses give the error in the last digit quoted.

Table 5. He II $\lambda 4686$ Equivalent Widths

HJD (-2,450,000)	Orbital Phase	W_λ (\AA)	ΔW_λ (\AA)	Run Number	X-ray State
52448.748 ..	0.276	-0.39	0.03	8	high/soft
52448.905 ..	0.304	-0.35	0.02	8	high/soft
52449.733 ..	0.452	-0.21	0.03	8	high/soft
52449.885 ..	0.479	-0.22	0.02	8	high/soft
52449.969 ..	0.494	-0.24	0.03	8	high/soft
52450.713 ..	0.627	-0.53	0.03	8	high/soft
52450.855 ..	0.653	-0.50	0.02	8	high/soft
52450.958 ..	0.671	-0.49	0.02	8	high/soft
52451.732 ..	0.809	-0.56	0.07	8	high/soft
52452.796 ..	0.999	-0.47	0.08	8	high/soft
52452.930 ..	0.023	-0.40	0.02	8	high/soft
52453.709 ..	0.162	-0.49	0.05	8	high/soft
52453.889 ..	0.194	-0.47	0.03	8	high/soft
52453.965 ..	0.208	-0.44	0.03	8	high/soft
52824.884 ..	0.445	-0.38	0.06	9	high/soft
52824.891 ..	0.447	-0.23	0.06	9	high/soft
52826.841 ..	0.795	-0.25	0.04	9	high/soft
52912.769 ..	0.140	-0.46	0.02	10	low/hard
52912.773 ..	0.140	-0.49	0.02	10	low/hard
52913.768 ..	0.318	-0.46	0.02	10	low/hard
52914.766 ..	0.496	-0.23	0.02	10	low/hard
52915.761 ..	0.674	-0.31	0.02	10	low/hard

Table 6. He II $\lambda 4686$ Equivalent Width Averages

Observation Dates (BY)	W_λ (\AA)	$\sigma(W_\lambda)$ (\AA)	Source
1971–1981	–0.36	0.12	Gies & Bolton (1986a)
1980–1984	–0.29	0.09	Ninkov et al. (1987)
1996–1998	–0.25	0.12	Brockopp et al. (1999)
2002–2003	–0.39	0.12	This paper, high/soft state
2003	–0.39	0.11	This paper, low/hard state

Table 7. Mean Flux Across the Wind Lines

HJD (-2,400,000)	Orbital Phase	Mean Flux (Si IV λ 1400)	Mean Flux (C IV λ 1550)	Source	X-ray State	Ref.
43629.222 ..	0.313	1.079	0.622	IUE	low	1,2,3
43629.917 ..	0.437	1.109	0.725	IUE	low	1,2,3
43630.898 ..	0.612	1.094	0.691	IUE	low	1,2,3
43632.884 ..	0.967	0.854	0.632	IUE	low	1,2,3
43636.069 ..	0.536	1.099	0.756	IUE	low	1,2,3
43638.907 ..	0.042	0.898	0.667	IUE	low	1,2,3
43701.758 ..	0.266	0.965	0.728	IUE	low	1,2,3
43708.857 ..	0.534	1.069	0.765	IUE	low	1,2,3
43799.446 ..	0.711	0.963	0.733	IUE	low	1,2,3
43802.485 ..	0.254	0.901	0.649	IUE	low	1,2,3
43804.629 ..	0.636	0.995	0.789	IUE	low	1,2,3
43845.978 ..	0.020	0.753	0.588	IUE	low	1,2,3
43848.020 ..	0.385	0.993	0.735	IUE	low	1,2,3
43892.220 ..	0.278	1.004	0.751	IUE	low	1,2,3
43894.744 ..	0.729	0.932	0.678	IUE	low	1,2,3
43894.811 ..	0.741	0.886	0.671	IUE	low	1,2,3
43896.419 ..	0.028	0.795	0.648	IUE	low	1,2,3
44002.919 ..	0.046	0.814	0.610	IUE	low	1,2,3
44003.118 ..	0.082	0.843	0.654	IUE	low	1,2,3
44003.259 ..	0.107	0.843	0.533	IUE	low	1,2,3
44035.011 ..	0.777	0.887	0.696	IUE	low	1,2,3
44265.582 ..	0.952	0.739	0.548	IUE	low	1,4
44412.390 ..	0.168	0.929	0.683	IUE	high	5
44416.117 ..	0.834	0.817	0.577	IUE	high	5
44419.259 ..	0.395	0.924	0.764	IUE	high	5
44419.797 ..	0.491	1.009	0.805	IUE	high	5
44422.310 ..	0.940	0.840	0.678	IUE	high	5,6
44423.302 ..	0.117	0.790	0.584	IUE	high	5,6
44425.301 ..	0.474	0.993	0.746	IUE	high	5,6
44426.941 ..	0.767	0.962	0.757	IUE	high	5,6

Table 7—Continued

HJD (-2,400,000)	Orbital Phase	Mean Flux (Si IV λ 1400)	Mean Flux (C IV λ 1550)	Source	X-ray State	Ref.
52450.272 ..	0.548	0.947	0.714	HST	high	7
52450.335 ..	0.560	0.947	0.722	HST	high	7
52453.210 ..	0.073	0.752	0.515	HST	high	7
52453.272 ..	0.084	0.761	0.520	HST	high	7
52825.702 ..	0.592	1.030	0.743	HST	high	7
52825.765 ..	0.603	1.014	0.725	HST	high	7
52827.702 ..	0.949	0.804	0.551	HST	high	7
52827.765 ..	0.960	0.787	0.530	HST	high	7

References. — 1. Ling et al. (1983); 2. Kemp, Barbour, & McBirney (1981); 3. Priedhorsky, Terrell, & Holt (1983); 4. Perotti et al. (1986); 5. Ogawara et al. (1982); 6. Oda (1980); 7. This paper.

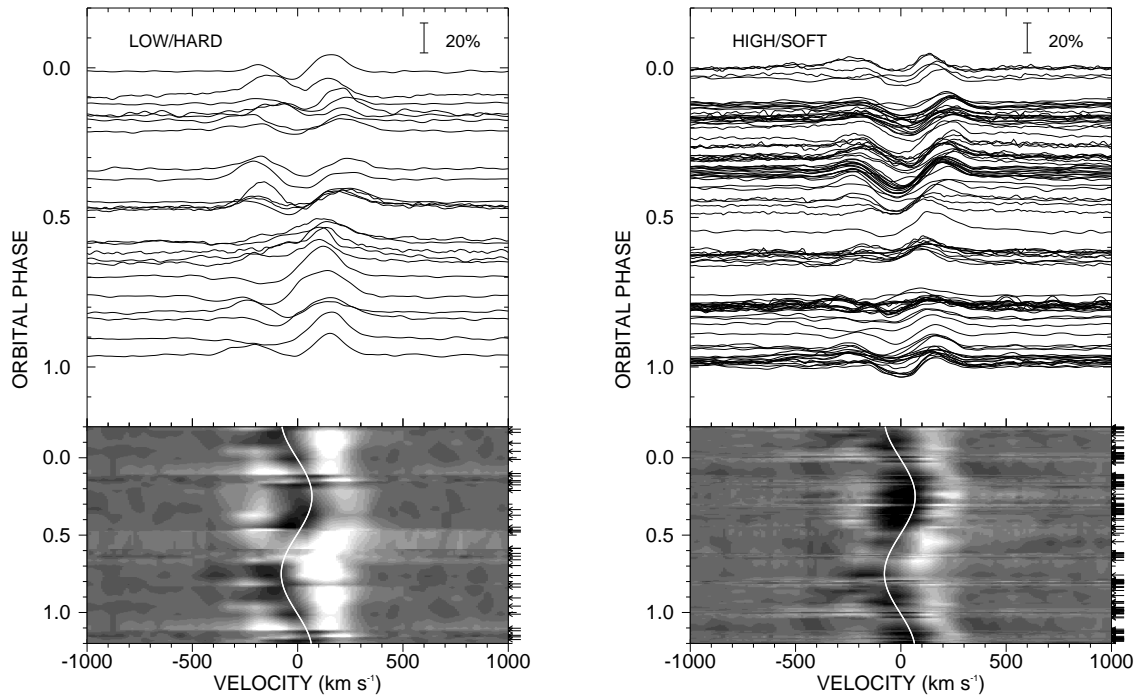


Fig. 1.— Two depictions of the $H\alpha$ profiles as a function of heliocentric radial velocity and orbital phase and grouped according to X-ray state at the time of observation. The X-ray high/soft group was selected from observations made between HJD 2,452,100 – 2,452,550 and between HJD 2,452,770 – 2,452,880, and all other times were assigned to the X-ray low/hard group (see Fig. 2). The upper panel in each shows the profiles with their continua aligned to the orbital phase of observation, while the lower panel is a grayscale version of the profiles with the first and last 20% of the orbit repeated to improve the sense of phase continuity. The grayscale intensities represent the rectified spectral flux between 0.92 (black) and 1.12 (white). The white line in the grayscale image shows the orbital velocity curve of the supergiant.

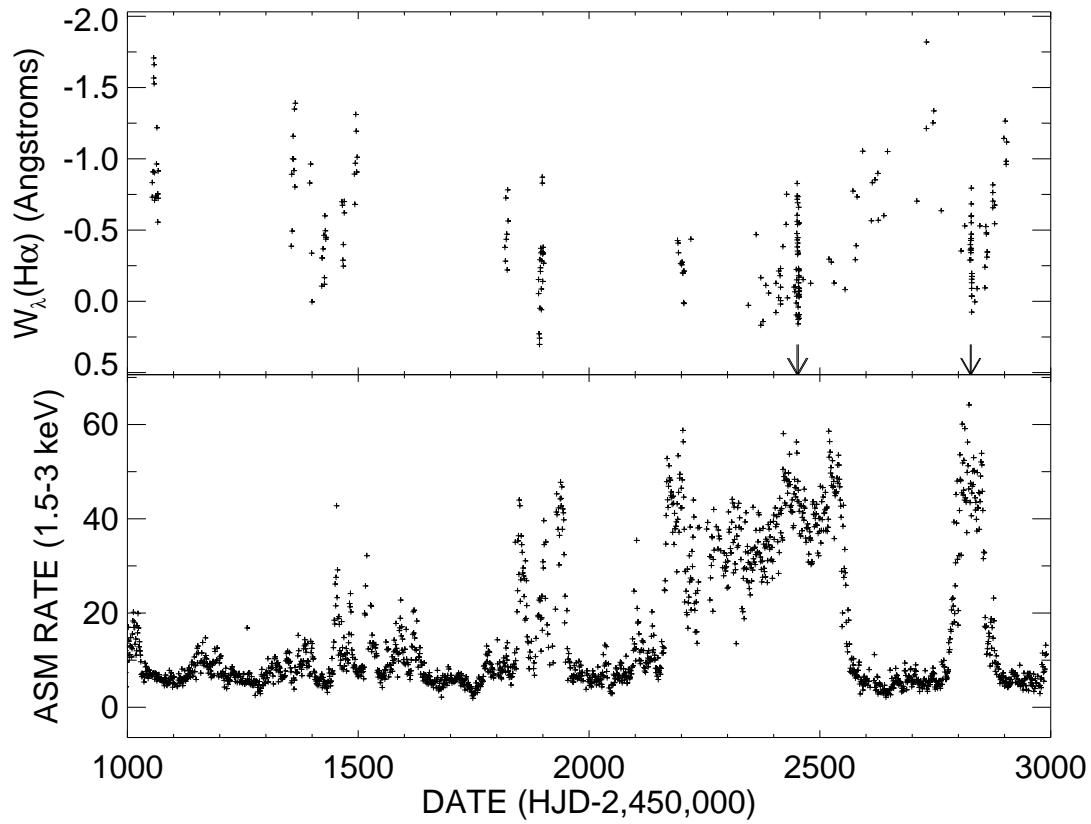


Fig. 2.— The long term variations in the H α emission strength (*above*) and daily average soft X-ray flux (*below*). The two arrows in the upper panel indicate the times of the STIS observations that occurred during the X-ray high/soft state. The recent, more densely sampled observations show clearly how the H α emission increases as the soft X-ray flux declines.

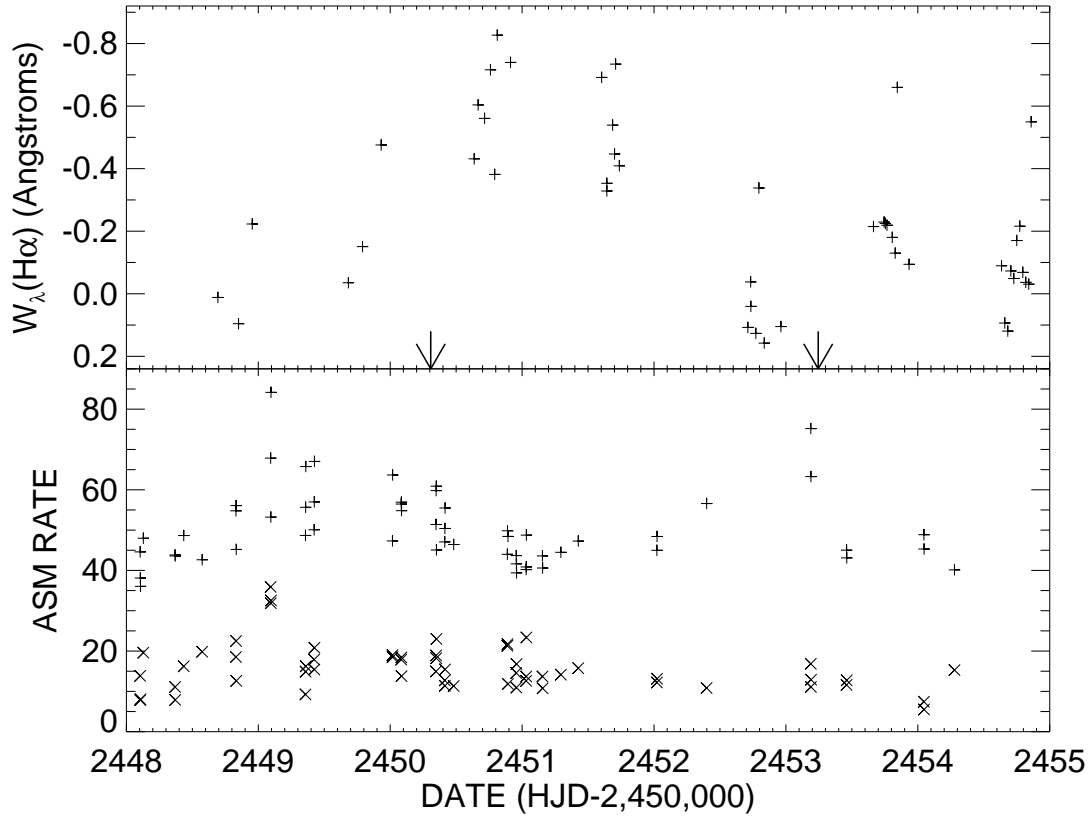


Fig. 3.— The variations in H α emission strength (*above*) and X-ray flux for each dwell observation (*below*) for the week surrounding the first *HST* run in 2002. The arrows in the top panel show the times of the STIS observations for each orbital conjunction phase. The symbols in the lower panel indicate the count rates in the 1.5 – 3 keV (+) and 5 – 12 keV (\times) bands.

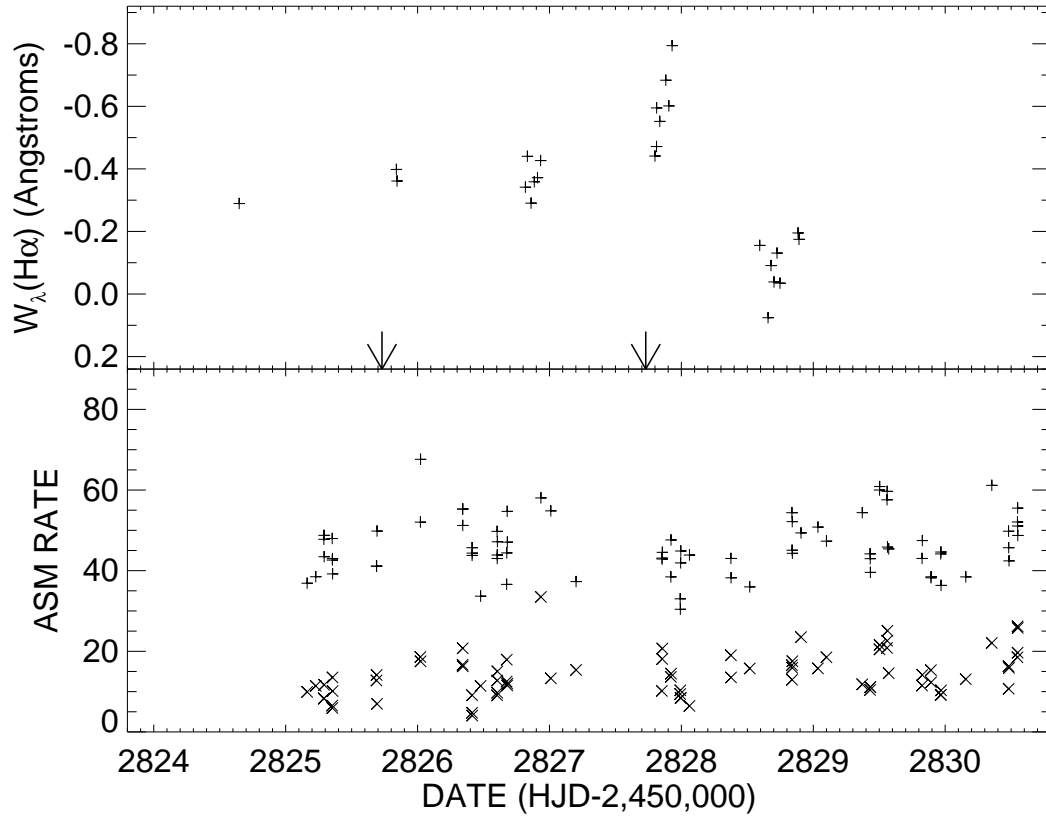


Fig. 4.— The variations in H α emission strength (*above*) and X-ray flux for each dwell observation (*below*) for the week surrounding the second *HST* run in 2003 (in the same format as Fig. 3).

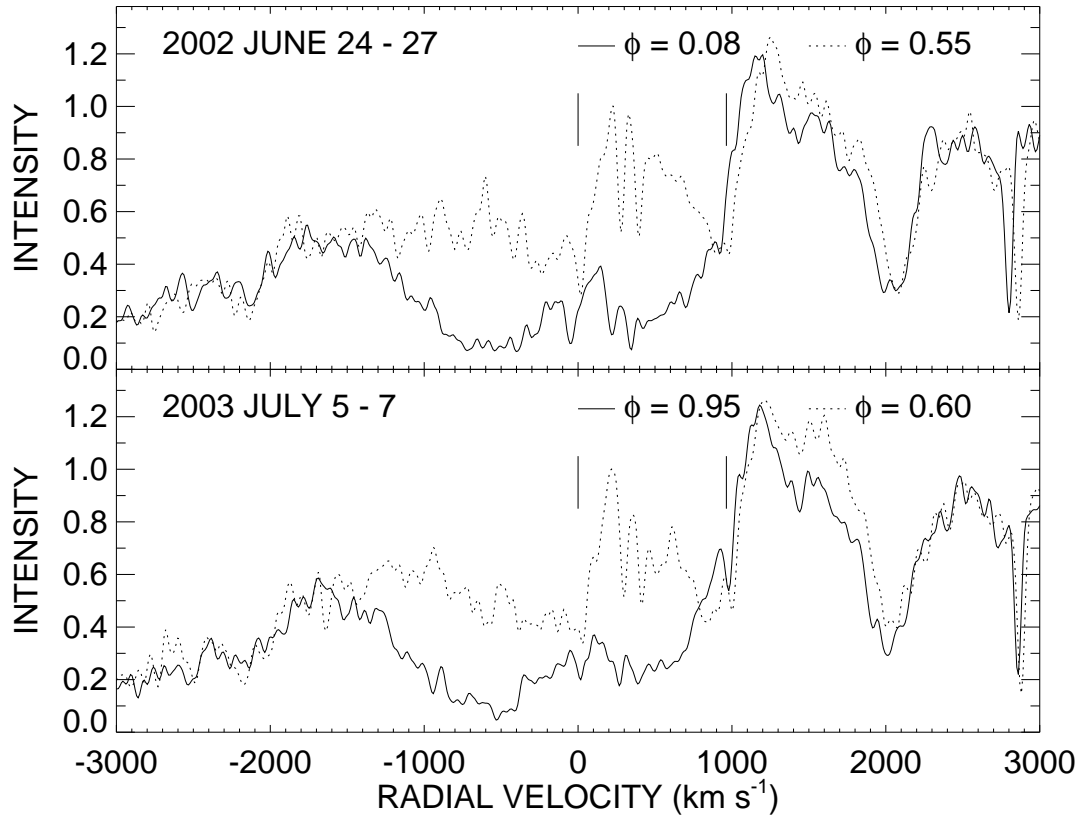


Fig. 5.— The spectral variations observed between conjunctions for the N V $\lambda\lambda 1238, 1242$ wind feature in both the 2002 (*top*) and 2003 (*bottom*) runs. The spectra are plotted as a function of Doppler shift for the blue component of the doublet in the rest frame of the supergiant (which leads to small offsets in the positions of the narrow, interstellar lines that are stationary in the absolute frame). Vertical line segments indicate the rest wavelength positions of both components of the doublet.

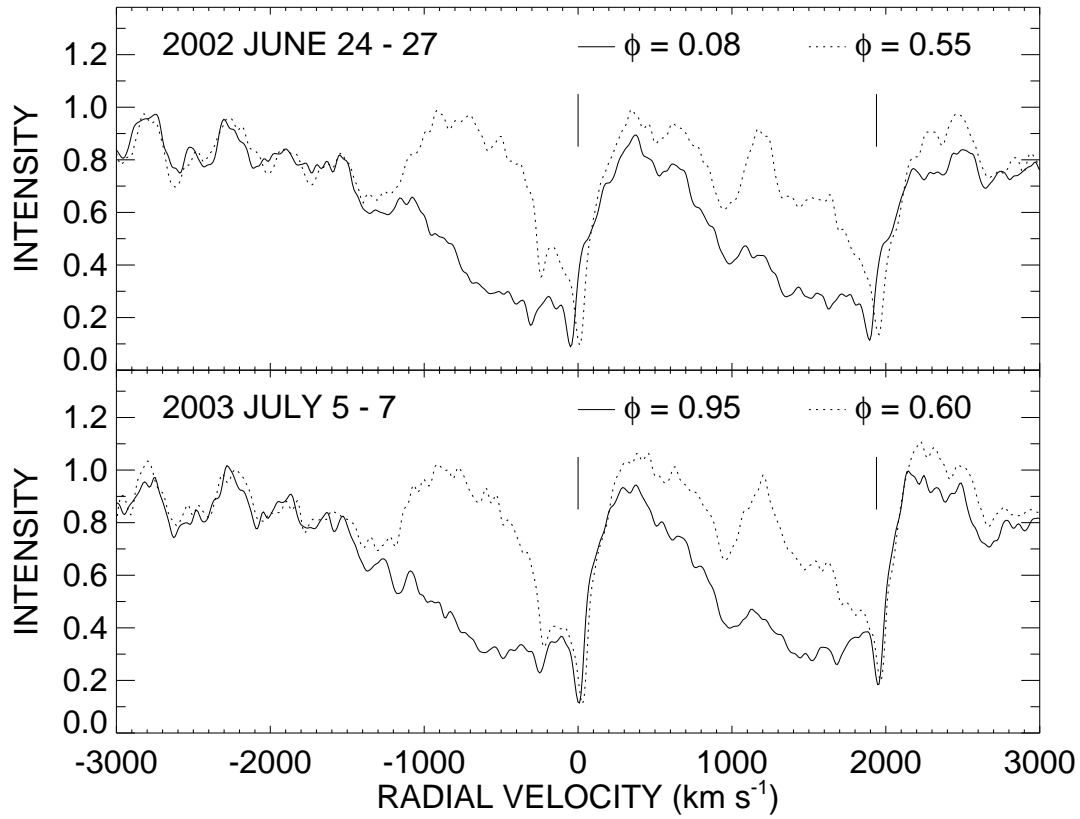


Fig. 6.— The spectral variations observed between conjunctions for the Si IV $\lambda\lambda 1393, 1402$ wind feature in the same format as Fig. 5.

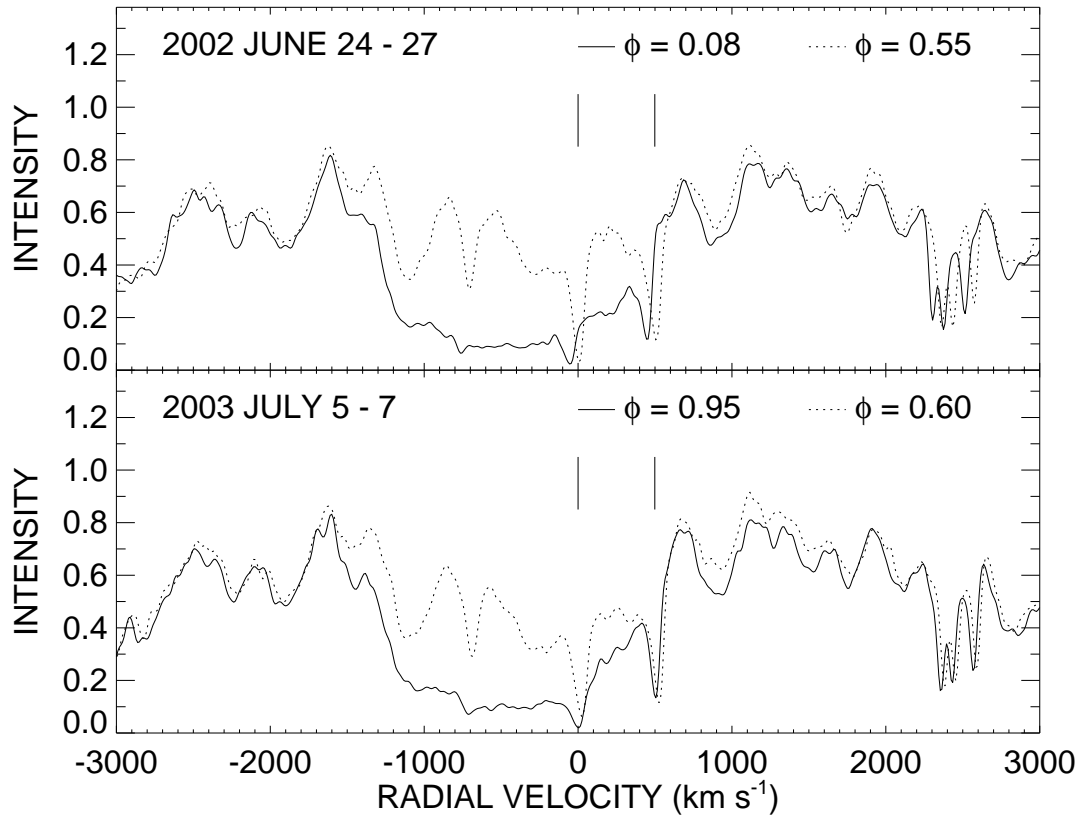


Fig. 7.— The spectral variations observed between conjunctions for the C IV $\lambda\lambda 1548, 1550$ wind feature in the same format as Fig. 5.

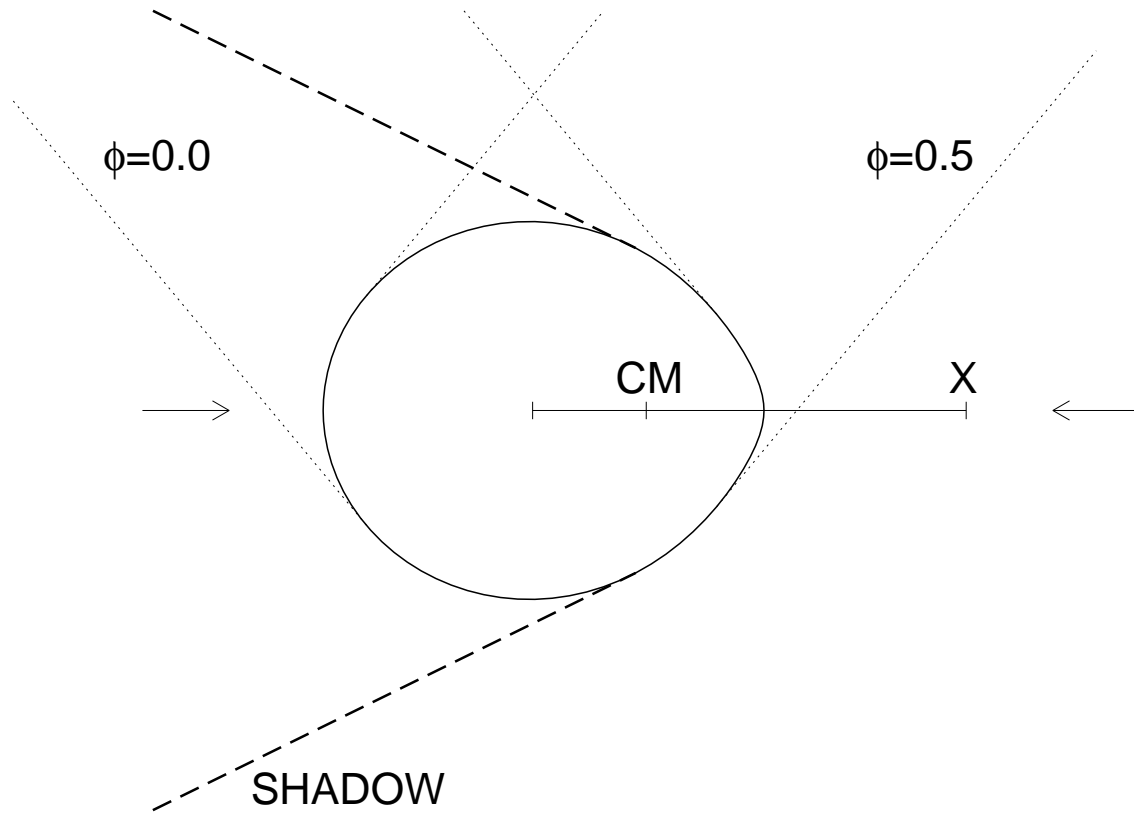


Fig. 8.— A cartoon view of the binary from within the orbital plane. The normal wind ions are assumed to exist only within the shadow wind zone to the left of the supergiant (bounded by a thick, dashed line) where the X-ray flux from the vicinity of the black hole (marked by “X”) is fully blocked, while the gas is ionized to higher levels in the rest of the wind. The simple model predictions are based upon viewing the system along the line of centers (shown by arrows), while in fact we observe the supergiant at a lower inclination angle ($i = 40^\circ$ assumed). The dotted lines show the part of the line of sight that is projected onto the disk of the star at the two orbital phases for an observer at the correct direction with respect to the orbital plane. The shadow wind region projected against the star in each case is the area bounded by the surface of the star and the dashed and dotted line for that phase. CM marks the center of mass position.

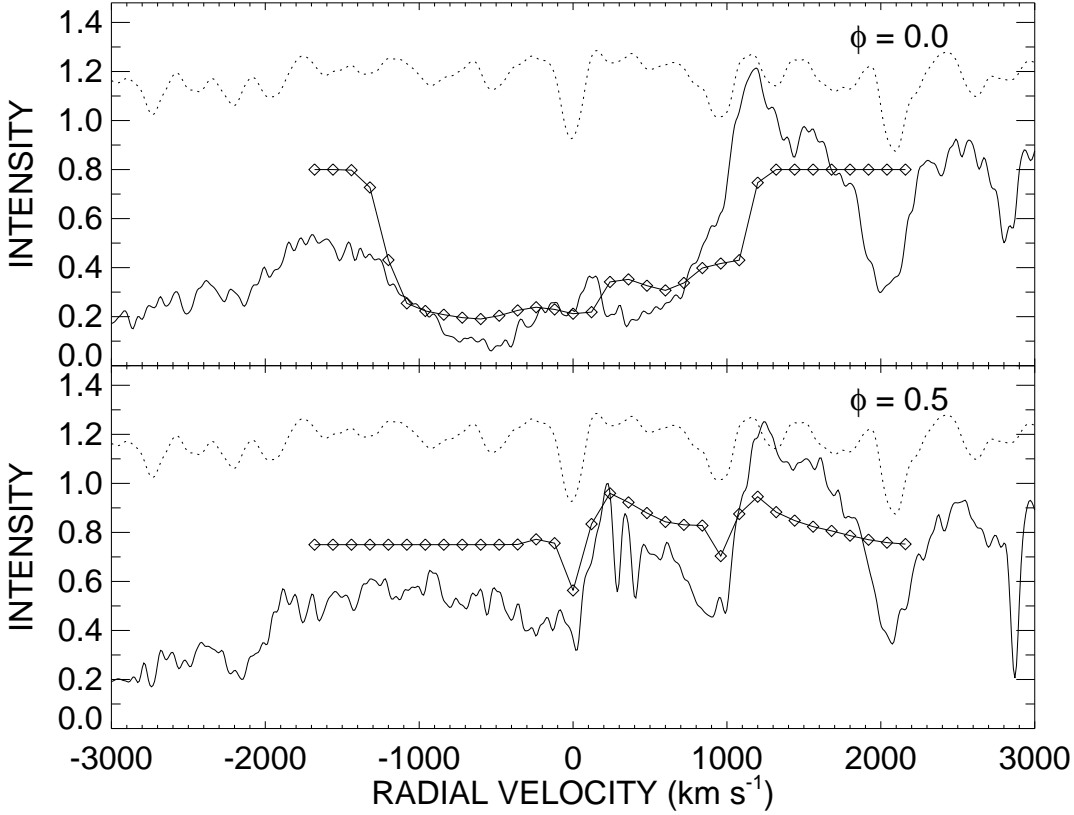


Fig. 9.— The average observed spectrum (*solid line*) and the shadow wind model spectrum (*connected diamonds*) for the N V $\lambda\lambda 1238, 1242$ wind feature (plotted as a function of Doppler shift for the blue component of the doublet in the rest frame of the supergiant). The top panel shows the profiles for case where the black hole is in the background while the bottom profile illustrates the other conjunction case where the black hole is in the foreground (photoionizing the wind gas seen projected against the supergiant). The dotted line shows the predicted photospheric line spectrum (offset for clarity) from the models of Lanz & Hubeny (2003). Note that the latter representation does not include the broad Ly α wings that depress the continuum in the observed spectrum towards the left hand side of the diagram.

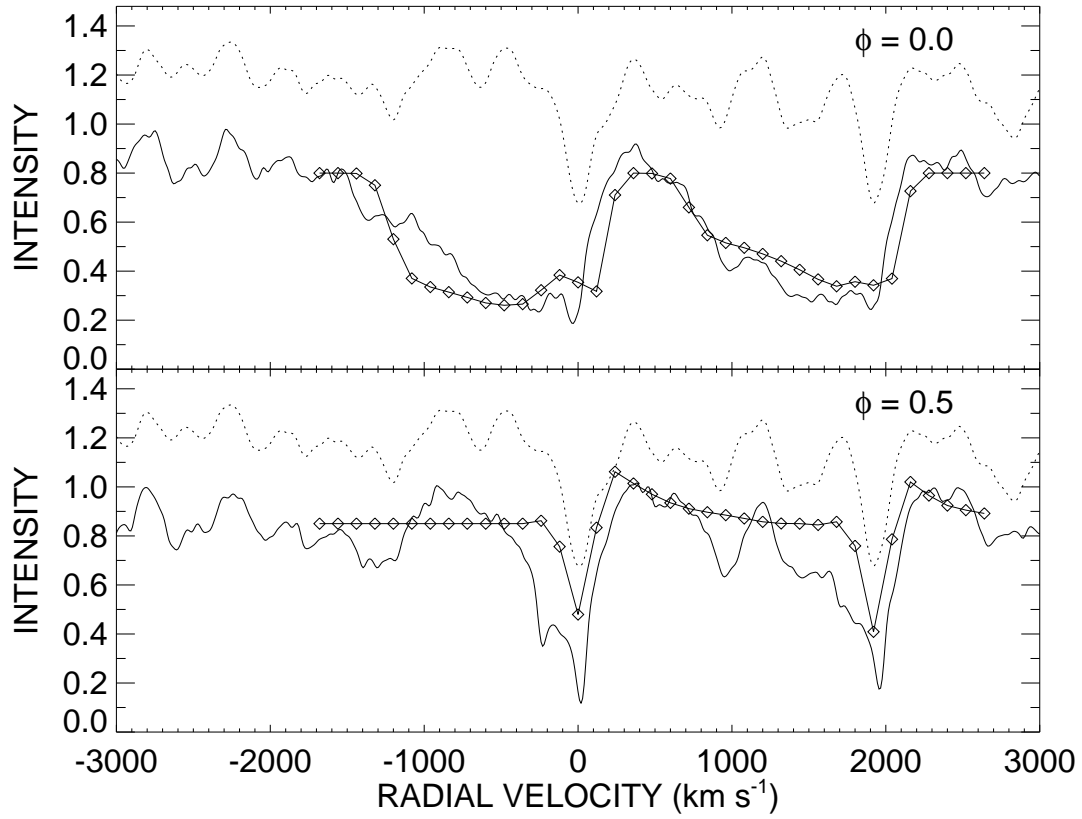


Fig. 10.— The average observed spectrum (*solid line*) and the shadow wind model spectrum (*connected diamonds*) for the Si IV $\lambda\lambda 1393, 1402$ wind feature in the same format as Fig. 9.

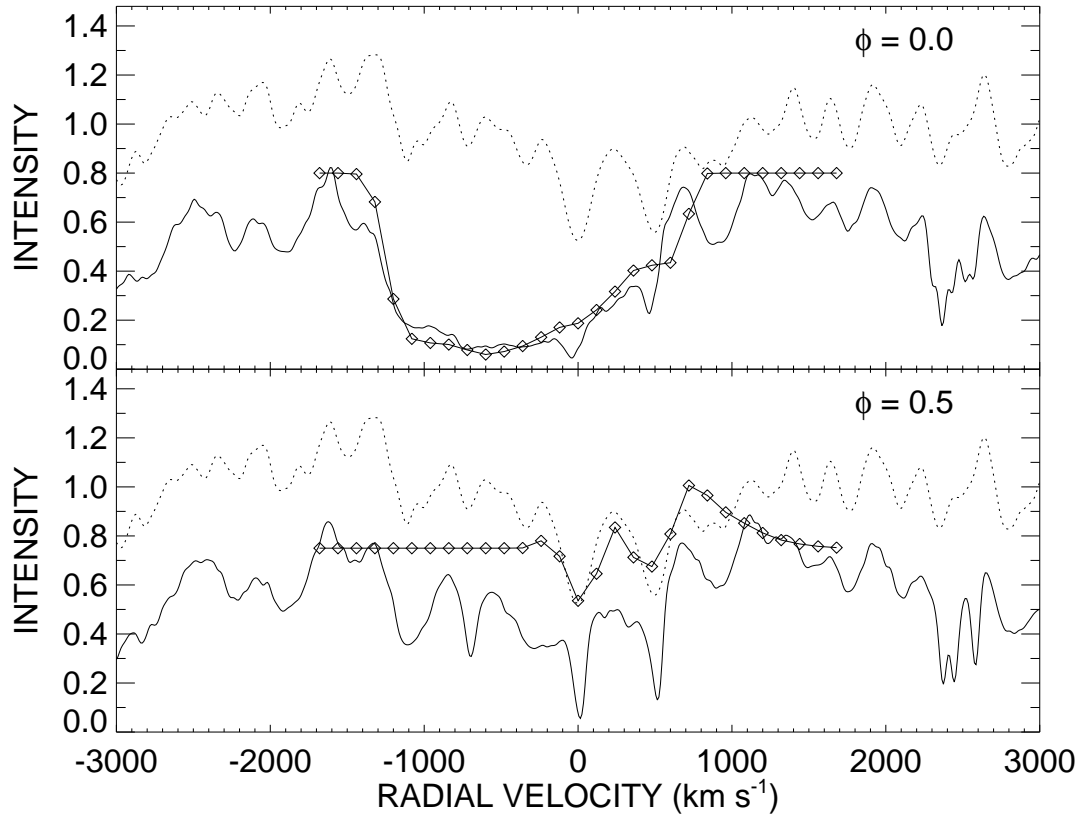


Fig. 11.— The average observed spectrum (*solid line*) and the shadow wind model spectrum (*connected diamonds*) for the C IV $\lambda\lambda 1548, 1550$ wind feature in the same format as Fig. 9.

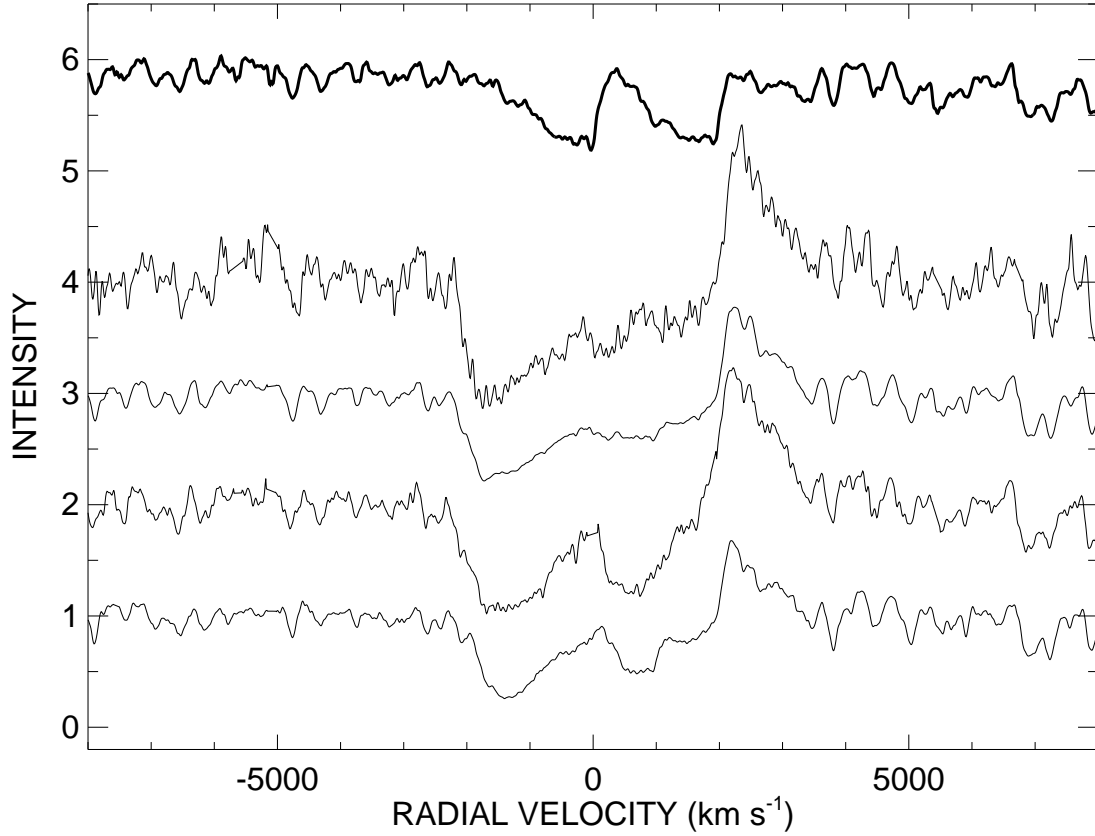


Fig. 12.— The mean Si IV wind profile for orbital phase $\phi = 0.0$ as a function of radial velocity for the blue member of the doublet. The spectrum of HD 226868 is plotted at the top as a thick line, and below are average spectra for other O9.7 Iab supergiants (offset in intensity for clarity). From top to bottom, these are HD 75222, HD 152003, HD 149038, and HD 167264.

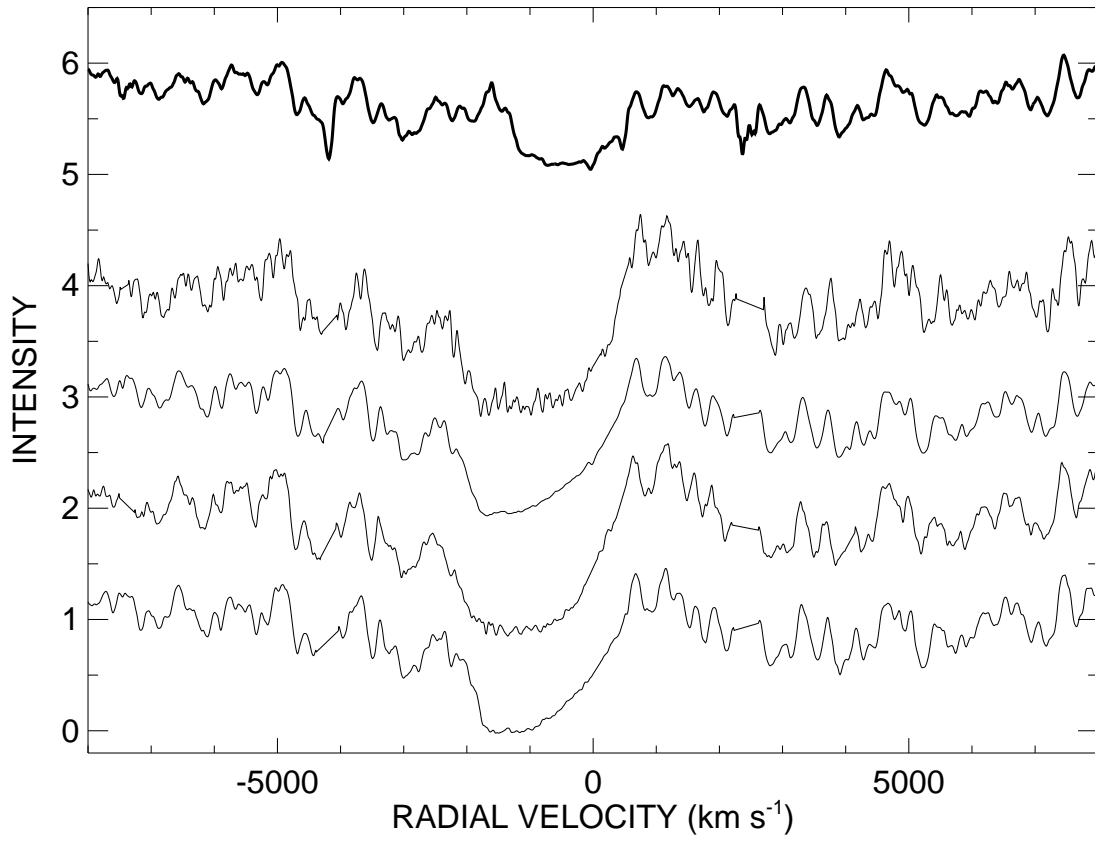


Fig. 13.— The mean C IV wind profile of HD 226868 for orbital phase $\phi = 0.0$ (*top, thick line*) compared to those of other O9.7 Iab supergiants (in the same format as Fig. 12).

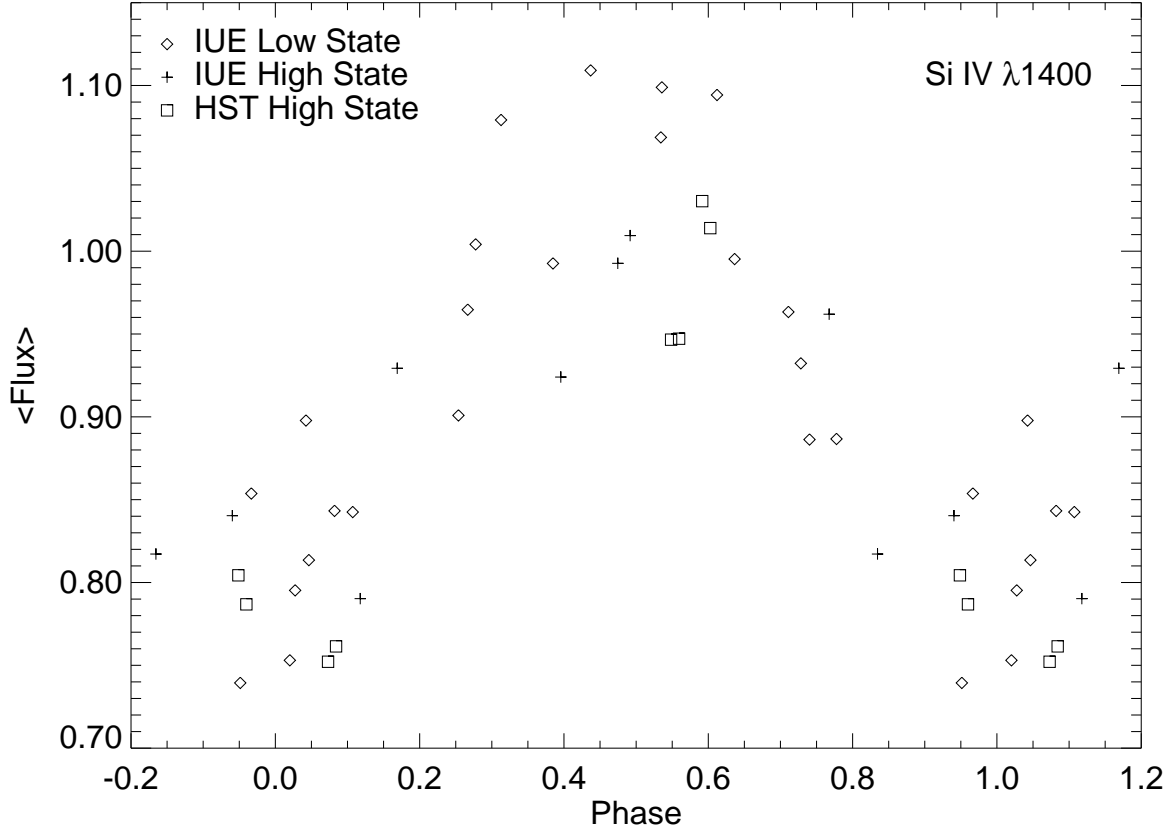


Fig. 14.— The mean flux across the Si IV wind profile plotted as a function of orbital phase. The different symbols represent measurements of *IUE* low/hard state (*diamonds*), *IUE* high/soft state (*plus signs*), and *HST* high/soft state spectra (*squares*). The Hatchett-McCray effect is seen as low flux (deep absorption) when the black hole is in the background and high flux (little absorption) when the black hole is in the foreground. The *IUE* flux measurements have a typical error of $\pm 7\%$.

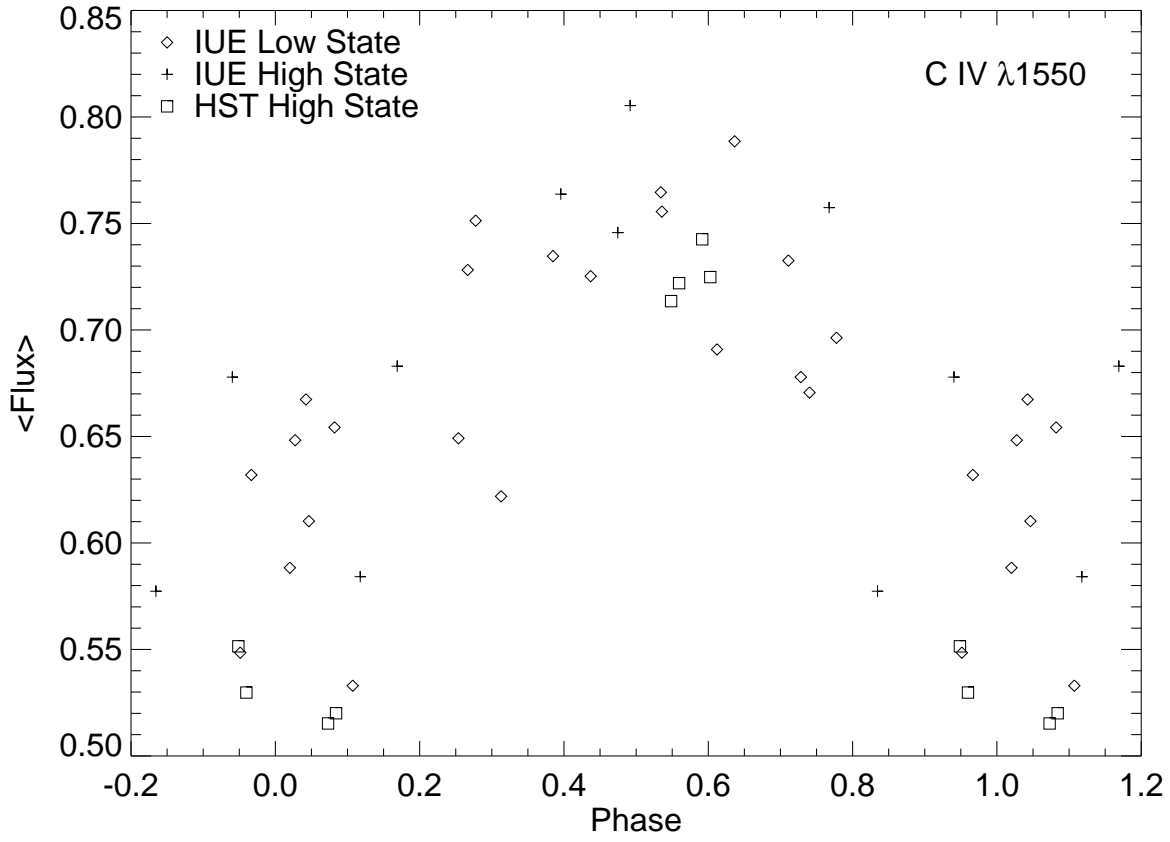


Fig. 15.— The mean flux across the C IV wind profile plotted as a function of orbital phase in the same format as Fig. 14.